



Contents lists available at ScienceDirect

# International Journal of Rock Mechanics & Mining Sciences

journal homepage: [www.elsevier.com/locate/ijrmms](http://www.elsevier.com/locate/ijrmms)

## Analysis of the classical pseudo-3D model for hydraulic fracture with equilibrium height growth across stress barriers

José I. Adachi<sup>a</sup>, Emmanuel Detournay<sup>b,c,\*</sup>, Anthony P. Peirce<sup>d</sup>

<sup>a</sup> Schlumberger Data & Consulting Services, USA

<sup>b</sup> Department of Civil Engineering, University of Minnesota, 500 Pillsbury Drive SE, Minneapolis, MN 55455, USA

<sup>c</sup> CSIRO Earth Science and Resource Engineering, Australia

<sup>d</sup> University of British Columbia, Canada

### ARTICLE INFO

#### Article history:

Received 14 July 2009

Received in revised form

13 February 2010

Accepted 10 March 2010

Available online 15 April 2010

#### Keywords:

Hydraulic fracture

P3D

Symmetric stress barriers

Equilibrium height growth

Collocation methods

### ABSTRACT

This paper deals with the so-called “pseudo three-dimensional” (P3D) model for a hydraulic fracture with equilibrium height growth across two symmetric stress barriers. The key simplifying assumptions behind the P3D model are that (i) each cross section perpendicular to the main propagation direction is in a condition of plane-strain, and (ii) the local fracture height is determined by a balance between the effect of the stress jump across the barriers and that of the rock toughness. Furthermore, in the equilibrium height growth P3D models, the pressure is assumed to be uniform in each vertical cross-section. We revisit this particular model by first formulating the non-linear differential equations governing the evolution of the length, height, and aperture of the hydraulic fracture, in contrast to the numerical formulations adopted in many previous studies. Scaling of these equations shows that the solution depends, besides the dimensionless space and time coordinates, on only two numbers representing a scaled toughness and a scaled leak-off coefficient. Analysis of the governing equations enables us to determine explicitly the conditions under which breakthrough takes place (i.e., the onset of growth into the bounding layers), as well as the conditions of unstable height growth (i.e., the conditions of “runaway height” when the main assumptions of the equilibrium height model become invalid). The mathematical model is solved numerically using a novel implicit fourth order collocation scheme on a moving mesh, which makes explicit use of the fracture tip asymptotics. We then report the results of several numerical simulations conducted for different values of the dimensionless toughness and the dimensionless leak-off coefficients, as well as a comparison with closed-form small and large time similarity solutions that are valid under conditions where the fracture remains contained within the reservoir layer.

© 2010 Elsevier Ltd. All rights reserved.

### 1. Introduction

This paper deals with the “pseudo-3D” (P3D) model of a hydraulic fracture, a model widely used in the petroleum industry to design stimulation treatments of underground hydrocarbon reservoirs by hydraulic fracturing. The P3D model was introduced in the 1980s [1–7], as an extension of the classical PKN (Perkins–Kern–Nordgren) model [8,9] to simulate the propagation of a vertical hydraulic fracture into a horizontally layered reservoir. Like the PKN model, the P3D model is applicable to situations in which the height of the fracture remains small compared to its length. However, in contrast to the PKN model, the height of the

P3D fracture is not limited to the reservoir thickness  $H$ , see Fig. 1. Indeed, the fracture is allowed to grow vertically into the adjacent layers confining the hydrocarbon bearing strata, but at a rate that is much smaller than the rate at which the fracture extends laterally, so as to justify the critical assumption of local elastic compliance, which is at the heart of the PKN and P3D models.

Solving the problem of an evolving planar hydraulic fracture is a challenging task, due in part to the moving boundary nature of this class of problems, the strong non-linearity introduced by the lubrication equation, the non-local relationship between the pressure in the fracture and its aperture, and the delay associated with leak-off of the fracturing fluid. While numerical algorithms have been developed to calculate the evolution of a planar hydraulic fracture in a layered geological medium [10–17], there are situations when the solution can be simplified and can thus be obtained with much less computational expense. In particular, the P3D model simplifies the form of the boundary curve  $C(t)$  that contains the evolving fracture footprint, by considering only the

\* Corresponding author at: Department of Civil Engineering, University of Minnesota, 500 Pillsbury Drive SE, Minneapolis, MN 55455, USA.

Tel.: +1 612 625 3043; fax: +1 612 626 7750.

E-mail address: [detou001@umn.edu](mailto:detou001@umn.edu) (E. Detournay).

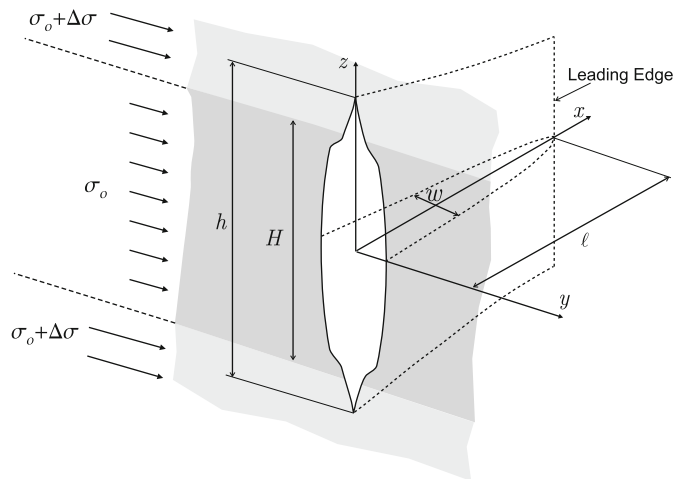


Fig. 1. Problem description.

horizontal extent of the fracture in the reservoir and the associated vertical penetration of the fracture into the adjacent layers.

The main distinguishing feature of both PKN and P3D models is the local nature of the fracture compliance, a consequence of assuming that the height/length ratio is small. In other words, the average fracture aperture in a vertical cross-section of a PKN or P3D model depends only on the fluid pressure in that cross-section, in contrast to planar fracture models [10,14,17,18] that are characterized by non-local interaction between the pressure and aperture fields. While for the PKN fracture the compliance is constant, a function only of the thickness of the reservoir layer and its elastic properties, the local compliance in the P3D model is itself part of the solution, as it depends on the local height of the fracture, which is *a priori* unknown. The local compliance and height of the fracture depend also on further assumptions about the pressure field in a vertical cross-section; the pressure is assumed to be uniform in the “equilibrium height” P3D model [3], but is calculated on account of a vertical flow in the “dynamic height” P3D model [5]. Nevertheless, allowing vertical fracture growth brings another non-linearity to the model—in addition to that which results from the dependence of the hydraulic conductivity on the fracture aperture in the lubrication equation governing the longitudinal viscous flow of fluid in the fracture.

As a result of these various assumptions, most of which have been inherited from the PKN model, the P3D hydraulic fracture is governed by a non-linear one-dimensional diffusion type equation over a domain that is evolving in time. In the equilibrium height P3D model, the focus of this investigation, this equation can be written explicitly, as shown later in this paper. Despite its strong non-linear nature, this partial differential equation can be solved at a small fraction of the computational cost required to simulate arbitrary shaped planar hydraulic fractures. The P3D model is therefore well suited to designing hydraulic fracturing treatments, when multiple scenarios have to be evaluated, provided that the assumptions upon which the model is built are respected.

Despite the importance of the P3D model for the design of hydraulic fracturing treatments, it does not appear, however, that this model has been rigorously formulated and scrutinized, as previous studies have generally emphasized either the discretized form of the governing equations—the so-called cell-based methods [7], and/or the application of the model to particular field cases. In particular, the conditions under which equilibrium height growth takes place, a critical assumption for the validity of the equilibrium height P3D model, have not been determined.

This paper adopts a different approach from previous publications, as it seeks not only to formulate the mathematical problem rigorously, but it also aims, through an emphasis on scaling analysis, to derive general results rather than specific ones applicable to a distinct set of parameters. For these reasons, we consider the simplest case of an equilibrium height P3D hydraulic fracture propagating in a reservoir layer bounded by two semi-infinite layers with the same elastic properties as the pay zone. Furthermore, we assume that the fracturing fluid is Newtonian and incompressible and that the injection rate is constant. These assumptions have been adopted so as not to distract from the main objective of the paper, which is to provide a rigorous formulation of the problem and scaling of the equations. Nonetheless, these assumptions can be relaxed without affecting the equations that determine the fracture height and the fracture compliance, a main focus of this paper, nor the fundamentals of the numerical algorithm used to solve the propagation problem.

## 2. Mathematical formulation

### 2.1. Problem definition

The geometry of a “pseudo-3D” hydraulic fracture is sketched in Fig. 1. A reservoir layer of thickness  $H$  is bounded by two semi-infinite layers assumed to have the same elastic properties as the reservoir. The minimum horizontal far-field stress in the reservoir is  $\sigma_0$  and there is a (positive) stress jump  $\Delta\sigma$  between the reservoir and the bounding layers. Injection of an incompressible Newtonian fluid of dynamic viscosity  $\mu$  at a constant volumetric rate  $Q_0$  in a borehole causes the propagation of a symmetric hydraulic fracture along the reservoir layer with limited height-growth into the bounding layers. The main assumptions behind this model are that (i) each cross-section perpendicular to the main propagation direction is in plane strain on account of  $h_{\max}/\ell$  being small (where  $h_{\max}$  is the maximum fracture height and  $\ell$  is the fracture half-length, i.e., the length of a wing) and that the fracture height varies “slowly” with distance from the borehole, (ii) the fluid pressure is uniform in each vertical cross-section, and (iii) the local fracture height  $h \geq H$  is an equilibrium height controlled, in general, by the stress jump across the layers and by the rock toughness.

Before stating the various assumptions that lead to the formulation of the P3D model, we introduce a Cartesian coordinate system with its origin located on the wellbore at the mid-height of the reservoir layer, with the  $x$ -axis contained in the plane of the fracture and the  $z$ -axis pointing upwards along the wellbore, see Fig. 1. With this choice of coordinates, both the  $x$ - and  $z$ -axes are axes of symmetry.

### 2.2. P3D model assumptions

The P3D model simplifies the solution of the evolution of the planar fracture in the layered elastic system through a series of assumptions that are discussed below.

**Assumption 1.** The leading edge of the fracture, which defines the maximum lateral extent of the fracture, is vertical and restricted to the reservoir layer, see Fig. 1; its position is defined by  $x = \ell(t)$ . The fracture height,  $h(x,t)$  is bounded below by  $H$  (and equal to  $H$  at the leading edge), and, in view of the problem symmetry, the vertical penetration,  $d$ , of the hydraulic fracture (if it takes place) in either bounding layer is thus equal to  $d = (h - H)/2$ . The fracture boundary is thus defined by the two functions  $\ell(t)$  and  $h(x,t) \geq H$ , with  $h(\ell,t) = H$ ; i.e., the footprint of one wing corresponds to  $0 \leq x \leq \ell(t)$ , and  $-h(x,t)/2 \leq z \leq h(x,t)/2$ .

**Assumption 2.** The vertical component  $q_z$  of the fluid flux is negligible compared to the horizontal component  $q_x$ , i.e.  $|q_z/q_x| \ll 1$ . For this reason, we simplify the notation by writing  $q = q_x$ . This assumption implies through Poiseuille's law, which governs the flow of the viscous fracturing fluid in the crack, that the pressure field  $p_f$  does not depend on the  $z$  coordinate; i.e.,  $p_f(x,t)$ . Clearly, this assumption requires that the rate of height growth  $\partial h/\partial t$  is much smaller than the horizontal velocity  $d\ell/dt$  of the leading edge; hence, the coherence of this assumption needs to be verified *a posteriori*, once the solution has been obtained.

**Assumption 3.** A condition of plane strain exists in any vertical plane ( $y,z$ ). Provided that  $h/\ell \ll 1$ , the plane strain assumption is a good approximation for most of the fracture, except within a region near the leading edge of order  $O(H)$  [19]. This assumption implies that the dependence of both the aperture field  $w$  and the fracture height  $h$  on the independent variables  $x$  and  $t$  is via the pressure field  $p_f(x,t)$ , i.e.,  $w(x,z,t) = w_p(z,p_f)$  and  $h(x,t) = h_p(p_f)$ . This assumption is alternatively referred to as the local elasticity assumption. The kinematic condition  $w=0$  at the leading edge  $x = \ell(t)$ , in conjunction with the local assumption, implies that  $p_f = \sigma_0$  at  $x = \ell(t)$ , which is obviously coherent with the previously stated assumption that  $h(\ell,t) = H$ . As is well-known, adopting the local assumption in the region near the leading edge precludes the consideration of any propagation criterion; this assumption has to be relaxed to properly account for a fracture propagation criterion at the leading edge [19].

**Assumption 4.** Fracturing fluid leak-off into the reservoir layer is treated in accordance with Carter's model [20], which assumes a one-dimensional diffusion process. The usual hypotheses behind this model are that (i) the fracturing fluid deposits a thin layer of relatively low permeability, known as the filter cake, on the fracture walls, at a rate proportional to the leak-off rate and (ii) the filtrate has enough viscosity to fully displace the fluid already present in the rock pores.

2.3. Mathematical model

Before proceeding with the formulation of the mathematical model, we recognize that the above set of assumptions enables one to rigorously formulate the model in terms of field quantities that depend only on the variables  $x$  and  $t$ . Indeed, the dependence of the aperture field  $w$  and the flux field  $q$  on the variables  $x$  and  $t$  only through the pressure field  $p_f(x,t)$  (or its gradient) actually implies that the model can be formulated in terms of an average aperture  $\bar{w}(x,t)$  and an average flux  $\bar{q}(x,t)$ , respectively, defined as

$$\bar{w} = \frac{1}{H} \int_{-h/2}^{h/2} w dz, \quad \bar{q} = \frac{1}{H} \int_{-h/2}^{h/2} q dz. \tag{1}$$

We note that both averages have been defined with respect to the reservoir layer height  $H$ ; hence  $\bar{w}H$  is the cross-sectional area of the fracture and  $\bar{q}H$  is the total flux through the fracture cross-section located at  $x$ .

2.3.1. Elastic relationship between local aperture and net pressure

One of the governing equations of the P3D model is a non-linear local relationship between the average aperture  $\bar{w}$  and the fluid pressure  $p_f$ , which is derived from elasticity. The non-linearity stems from the dependence of the fracture height on the pressure, since the fracture growth in the vertical direction is subject to the requirement that the fracture is in a state of critical equilibrium, assuming that such equilibrium state exists. The relationship between  $\bar{w}$  and  $p_f$  can be derived by combining the integral equation that expresses the fracture aperture  $w(z)$  in terms of the net crack loading, the integral expression for the

stress intensity factor  $K_I$  in terms of the net crack loading [21–23], and the propagation criterion  $K_I = K_{Ic}$  [24,25], i.e.,

$$w = \frac{4}{\pi E'} \left[ p \int_0^{H/2} G(s,z) ds + (p - \Delta\sigma) \int_{H/2}^{h/2} G(s,z) ds \right], \tag{2}$$

$$K_I = \sqrt{\frac{8h}{\pi}} \left[ p \int_0^{H/2} \frac{ds}{\sqrt{h^2 - 4s^2}} + (p - \Delta\sigma) \int_{H/2}^{h/2} \frac{ds}{\sqrt{h^2 - 4s^2}} \right], \tag{3}$$

$$K_I = K_{Ic}, \tag{4}$$

where  $E' = E/(1 - \nu^2)$  is the plane strain Young's modulus,  $p$  is the net pressure defined as  $p = p_f - \sigma_0$  and  $G(s,z)$  is the elasticity kernel given by

$$G(s,z) = \ln \left| \frac{\sqrt{h^2 - 4z^2} + \sqrt{h^2 - 4s^2}}{\sqrt{h^2 - 4z^2} - \sqrt{h^2 - 4s^2}} \right|. \tag{5}$$

Eq. (5) for the kernel  $G(s,z)$  can be derived from the expression given by [26, (p. 5.10a)] for the fracture aperture at  $s$  due to a pair of opposed unit forces applied on the fracture faces at  $z$ . Since the kernel  $G$  can be integrated in closed form according to

$$\begin{aligned} \int G(s,z) ds &= \sqrt{h^2 - 4z^2} \arcsin\left(\frac{2s}{h}\right) \\ &\quad - z \ln \left| \frac{s\sqrt{h^2 - 4z^2} + z\sqrt{h^2 - 4s^2}}{s\sqrt{h^2 - 4z^2} - z\sqrt{h^2 - 4s^2}} \right| \\ &\quad + s \ln \left| \frac{\sqrt{h^2 - 4z^2} + \sqrt{h^2 - 4s^2}}{\sqrt{h^2 - 4z^2} - \sqrt{h^2 - 4s^2}} \right|. \end{aligned} \tag{6}$$

The fracture profile  $w(z)$  can be calculated explicitly for a given fracture height  $h$

$$\begin{aligned} w = \frac{2}{E'} (p - \Delta\sigma) \sqrt{h^2 - 4z^2} + \frac{4\Delta\sigma}{\pi E'} \left\{ \sqrt{h^2 - 4z^2} \arcsin\left(\frac{H}{h}\right) \right. \\ \left. - z \ln \left| \frac{H\sqrt{h^2 - 4z^2} + 2z\sqrt{h^2 - H^2}}{H\sqrt{h^2 - 4z^2} - 2z\sqrt{h^2 - H^2}} \right| + \frac{H}{2} \ln \left| \frac{\sqrt{h^2 - 4z^2} + \sqrt{h^2 - H^2}}{\sqrt{h^2 - 4z^2} - \sqrt{h^2 - H^2}} \right| \right\}. \end{aligned} \tag{7}$$

Furthermore, a closed-form expression relating the equilibrium height  $h$  and the net pressure is readily deduced from (3) and (4) [27]

$$2\arcsin\left(\frac{H}{h}\right) - \left(1 - \frac{p}{\Delta\sigma}\right)\pi = \sqrt{\frac{2\pi K_{Ic}}{H \Delta\sigma}} \sqrt{\frac{H}{h}}. \tag{8}$$

From (7) and (8), the relationship between  $\bar{w}$  and  $p$  can then be obtained in the form of a parametric equation in terms of  $h$ . Formally, this equation reads

$$\bar{w} = \bar{w}(h), \quad p = p(h). \tag{9}$$

The details of the derivation are given after scaling of the equations. We note, however, that in the particular case of the PKN model  $h=H$  and the fracture opening adopts an elliptical shape; hence (9) degenerates into the linear relation  $\bar{w} = M_0 p$ , with the compliance  $M_0 = \pi H/2E'$ .

2.3.2. Poiseuille's law

Next, we consider the relationship between the average flux  $\bar{q}$  and the pressure gradient. According to Poiseuille's law, the local flux  $q(z,t)$  is related to the pressure gradient by

$$q = -\frac{w^3}{12\mu} \frac{\partial p}{\partial x}, \quad -\frac{h}{2} < z < \frac{h}{2} \tag{10}$$

which after integration over  $h$  yields

$$\bar{q} = -\frac{\psi' \bar{w}^3}{\mu} \frac{\partial p}{\partial x}, \quad (11)$$

where  $\psi'$  is a shape factor that depends on the aperture profile and on the fracture height. The dependence of  $\psi'$  on the problem parameters will be discussed in the Scaling section. We simply note here that for the PKN model ( $h=H$ ),  $\psi' = \psi'_0 = \pi^{-2}$ .

### 2.3.3. Conservation law

The final governing equation is the local volume balance condition

$$\frac{\partial \bar{q}}{\partial x} + \frac{\partial \bar{w}}{\partial t} + \frac{C'}{\sqrt{t-t_0(x)}} = 0, \quad (12)$$

where  $t_0(x)$  is the time at which the crack leading edge arrives at coordinate  $x$ . The coefficient  $C' = 2C_l$  is the usual Carter leak-off coefficient  $C_l$  [20] multiplied by a factor 2 to account for leak-off through both walls of the fracture.

### 2.3.4. Boundary conditions

The governing equations (9), (11), and (12) are complemented by boundary conditions at the leading edge of the fracture,  $x = \ell(t)$

$$\bar{w}(\ell, t) = \bar{q}(\ell, t) = 0, \quad h(\ell, t) = H \quad (13)$$

and at the inlet

$$\bar{q}(0, t) = Q_0/2H. \quad (14)$$

Together with initial conditions to be discussed below, this set of equations are sufficient to determine the evolution of the fracture footprint defined by the two functions  $\ell(t)$  and  $h(x, t)$ , and the field quantities  $\bar{w}(x, t)$ ,  $p(x, t)$ , and  $\bar{q}(x, t)$ .

## 3. Dimensionless formulation

### 3.1. Scaling

Scaling of the governing equations is carried out by expressing the time and space variables and the dependent field variables, each as the product of a characteristic quantity and a dimensionless variable. In contrast to a scaling based on time-dependent characteristic quantities [28], the scaling introduced here relies on constant quantities, which leads to a form of equations that is more appropriate for numerical solution. So let  $\ell_*$ ,  $h_*$ , and  $t_*$ , respectively, denote the characteristic height and length of the fracture, and the characteristic time; and  $w_*$ ,  $p_*$ , and  $q_*$  the characteristic aperture, net pressure, and flow rate. The introduction of these characteristic quantities allows us to define the following dimensionless variables:

$$\xi = \frac{x}{\ell}, \quad \zeta = \frac{z}{h_*}, \quad \tau = \frac{t}{t_*}, \quad \gamma = \frac{\ell}{\ell_*}, \quad \lambda = \frac{h}{h_*}, \quad \Pi = \frac{p}{p_*},$$

$$\Psi = \frac{q}{q_*}, \quad \bar{\Psi} = \frac{\bar{q}}{q_*}, \quad \Omega = \frac{w}{w_*}, \quad \bar{\Omega} = \frac{\bar{w}}{w_*}. \quad (15)$$

Note that  $\xi$  is a stretching coordinate with  $\xi = 0$  corresponding to the fracture inlet and  $\xi = 1$  to the fracture tip, while  $\zeta$  is a fixed coordinate with  $-\lambda/2 \leq \zeta \leq \lambda/2$ .

The six characteristic quantities that have been introduced are identified by setting to unity, six of the dimensionless groups that emerge from the governing equations when they are expressed in terms of the dimensionless variables. The remaining two groups are numbers that control the problem.

After some algebraic manipulation, we obtain the following expressions for the characteristic quantities:

$$\ell_* = \frac{\pi H^4 \Delta \sigma^4}{4E^3 \mu Q_0}, \quad h_* = H, \quad t_* = \frac{\pi^2 H^6 \Delta \sigma^5}{4\mu E^4 Q_0^2}, \quad p_* = \Delta \sigma, \quad q_* = \frac{Q_0}{2H},$$

$$w_* = \frac{\pi H \Delta \sigma}{2E} = M_0 \Delta \sigma. \quad (16)$$

Therefore the solution of the problem consists of determining the net pressure  $\Pi(\xi, \tau)$ , the average aperture  $\bar{\Omega}(\xi, \tau)$ , and the flow rate  $\bar{\Psi}(\xi, \tau)$  in the evolving domain defined by the fracture length  $\gamma(\tau)$  and by the fracture height profile  $\lambda(\xi, \tau)$ . This solution depends also on two numbers, namely the dimensionless toughness  $\mathcal{K}$  of the bounding layers and the dimensionless leak-off coefficient  $C$  of the reservoir

$$\mathcal{K} = \sqrt{\frac{2\pi}{H}} \frac{K_{Ic}}{\Delta \sigma}, \quad (17)$$

$$C = \frac{C' H^2 \Delta \sigma^{3/2}}{\mu^{1/2} E' Q_0}. \quad (18)$$

Considering that, in most practical situations,  $H \sim 10-100$  m,  $\Delta \sigma \sim 0.1-10$  MPa,  $K_{Ic} \sim 0.1-1$  MPa m<sup>1/2</sup>,  $E' \sim 10^3-10^4$  MPa,  $\mu \sim 10^{-5}-10^{-4}$  MPa s,  $C' \sim 10^{-6}-10^{-3}$  m s<sup>1/2</sup>, and  $Q_0 \sim 10^{-3}-10^{-1}$  m<sup>3</sup>/s, then  $C$  and  $\mathcal{K}$  will generally vary between  $10^{-2}$  and 1. As we will discuss in a later section, the number  $C$  is related to a ratio of two timescales.

### 3.2. Equilibrium height

We can now formulate the mathematical model in dimensionless form. First, the relationship between the fracture height  $\lambda$ , the net pressure  $\Pi$ , and the toughness  $\mathcal{K}$  is deduced from (8) to be

$$\Pi = 1 - \frac{2}{\pi} \arcsin\left(\frac{1}{\lambda}\right) + \frac{\mathcal{K}}{\pi \sqrt{\lambda}}. \quad (19)$$

For the particular case of zero toughness, we obtain

$$\lambda = \csc\left[\frac{\pi}{2}(1-\Pi)\right], \quad \mathcal{K} = 0. \quad (20)$$

With the exception of  $\mathcal{K} = 0$ , the pressure  $\Pi$  is not a monotonic function of  $\lambda$ . Indeed, according to (19),  $\Pi$  achieves a maximum value when  $\lambda = \lambda_u$ , given by

$$\lambda_u = \frac{8 + \sqrt{\mathcal{K}^4 + 64}}{\mathcal{K}^2}, \quad \mathcal{K} > 0. \quad (21)$$

The decrease of  $\Pi$  with  $\lambda$  for  $\lambda > \lambda_u$  can readily be explained as follows. As  $\lambda$  becomes relatively large (and  $\mathcal{K} > 0$ ), the fracture asymptotically approaches the shape of a ‘‘Griffith’s crack,’’ i.e., a fracture subjected to a uniform net pressure. In other words, the contribution of the loading in the reservoir layer to the stress intensity factor becomes less relevant for increasing  $\lambda$ . For a Griffith’s crack of length  $h$  in critical equilibrium with a uniform net pressure  $p' = p - \Delta \sigma$ , the toughness, length and pressure are related according to  $\Pi = \mathcal{K}/\pi \sqrt{\lambda} + 1$  (using scaling (17)), which is exactly the dominant term in (19) for large  $\lambda$ , since  $\arcsin(1/\lambda) \sim 1/\lambda + O(\lambda^{-3})$  for  $\lambda \gg 1$ . Thus it is expected that the pressure  $\Pi$  should eventually decay as  $\sim 1/\sqrt{\lambda}$ .

The main implication of the above result is that unstable height growth is expected to take place once  $\lambda > \lambda_u$ . We will assume that  $\lambda > \lambda_u$  is indeed the criterion of instability, on noting that the net pressure increases with time according to numerical simulations. A formal argument, however, would require us to prove that  $\partial \Pi / \partial \tau > 0$  in the vertical cross-section where the height becomes unstable. The equilibrium height P3D model is obviously not valid once this critical height is exceeded, as one of the assumptions, namely that the rate of flow (or fracture

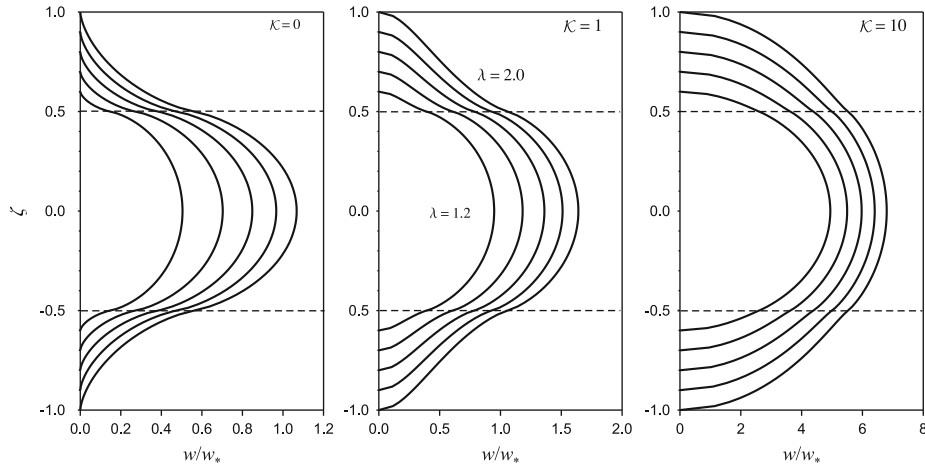


Fig. 2. Plots of  $w/w_*$  versus vertical coordinate  $\zeta$ , for different values of toughness  $\kappa$  and equilibrium height  $\lambda$  ( $\lambda = 1.2, 1.4, 1.6, 1.8$  and  $2.0$ ).

propagation) in the vertical direction is much less than the rate of flow in the horizontal direction, is then violated. The possibility of unstable height growth is mentioned in [27], but no criterion for calculating the critical height is given in that paper. A thorough discussion of pressure decline during injection as a symptom of unstable height growth can be found in [29].

### 3.3. Fracture compliance

After eliminating the pressure  $\Pi$  using the equilibrium height equation (19), the scaled opening profile  $\Omega(\zeta)$  can be deduced from (7)

$$\Omega = \frac{8}{\pi^2} \left[ \frac{\kappa}{2\sqrt{\lambda}} \sqrt{\lambda^2 - 4\zeta^2} - 2\zeta \ln \left| \frac{\sqrt{\lambda^2 - 4\zeta^2} + 2\zeta\sqrt{\lambda^2 - 1}}{\sqrt{\lambda^2 - 4\zeta^2} - 2\zeta\sqrt{\lambda^2 - 1}} \right| + \ln \left| \frac{\sqrt{\lambda^2 - 4\zeta^2} + \sqrt{\lambda^2 - 1}}{\sqrt{\lambda^2 - 4\zeta^2} - \sqrt{\lambda^2 - 1}} \right| \right] \quad (22)$$

We observe that the two logarithmic terms in (22) each become singular at the points  $\zeta = \pm 1/2$ , however, when combined they tend to the limiting value  $\ln \lambda$  so that  $\Omega$  remains continuous. A large  $\lambda$  asymptotic expression for  $\Omega$  can readily be derived from (22) as

$$\Omega \approx \frac{4}{\pi^2} \left[ \left( \frac{\kappa}{\sqrt{\lambda}} \right) \sqrt{\lambda^2 - 4\zeta^2} + O\left(\frac{1}{\lambda^3}\right) \right], \quad 1 \ll \zeta < \lambda.$$

This asymptotic expression for the fracture aperture can alternatively be obtained by superposing the aperture corresponding to a uniform equilibrium pressure in the fracture and the solution for a unit force dipole that accounts for the reduced confining stress across the reservoir layer. Plots of  $\Omega(\zeta)$  for different values of  $\lambda$  and  $\kappa$  are shown in Fig. 2.

The average opening  $\bar{\Omega}$ , defined as

$$\bar{\Omega} = 2 \int_0^{\lambda/2} \Omega(\zeta) d\zeta,$$

can then be calculated by integrating (22), which yields

$$\bar{\Omega} = \frac{1}{\pi} \left( \kappa \lambda^{3/2} + 2\sqrt{\lambda^2 - 1} \right), \quad \lambda > 1. \quad (23)$$

It is convenient to introduce the function  $c(\lambda; \kappa)$  defined as

$$c = \frac{\bar{\Omega}}{\Pi}. \quad (24)$$

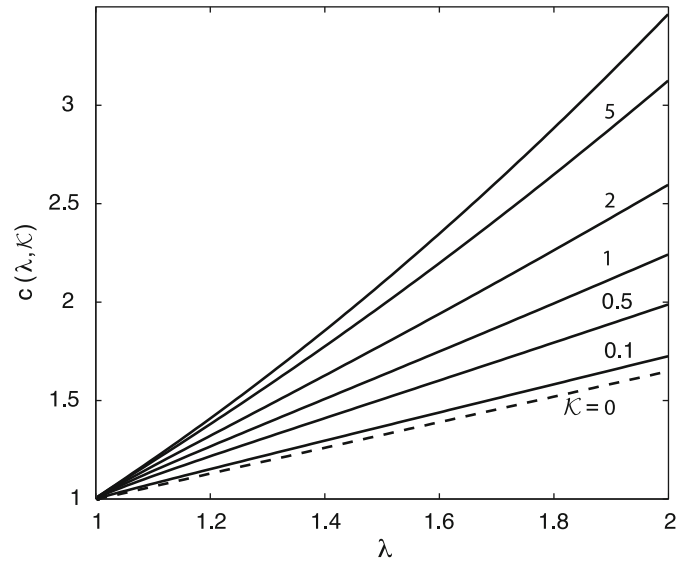


Fig. 3. Plot of compliance function  $c(\lambda; \kappa)$  for different values of dimensionless toughness  $\kappa$ . The dashed line corresponds to  $\kappa = 0$ .

The function  $c(\lambda; \kappa)$  is actually a “compliance correction function” as the fracture compliance  $M = \bar{w}/p$  can be expressed as

$$M = c(\lambda; \kappa)M_0.$$

Thus  $c(\lambda; \kappa)$  adjusts the elastic compliance at any given vertical section of the fracture to account for the height growth. Using (23) and (19), the latter to express  $\Pi$  as a function of  $\lambda$  and  $\kappa$ ,  $c(\lambda; \kappa)$  is given explicitly by

$$c(\lambda; \kappa) = \frac{\sqrt{\lambda}(\kappa \lambda^{3/2} + 2\sqrt{\lambda^2 - 1})}{\kappa + \sqrt{\lambda}[\pi - 2\arcsin(\frac{1}{\lambda})]}. \quad (25)$$

The function  $c(\lambda; \kappa)$  is a regular, strictly positive function, with  $c(1; \kappa) = 1$  and is unbounded for  $\lambda \rightarrow \infty$ . Plots of this function for different values of dimensionless toughness  $\kappa$  are shown in Fig. 3. For  $\kappa = 0$ , the compliance correction  $c$  can also be directly expressed as a function of  $\Pi$ , i.e.,

$$c = \frac{2}{\pi\Pi} \tan\left(\frac{\pi\Pi}{2}\right), \quad \kappa = 0.$$

Equivalently, combination of (20) and (23) allows us to derive the following direct relation between  $\bar{\Omega}$  and  $\Pi$  for  $\mathcal{K} = 0$ :

$$\frac{\pi}{2}\bar{\Omega} = \tan\left(\frac{\pi}{2}\Pi\right), \quad \mathcal{K} = 0. \tag{26}$$

### 3.4. Viscous flow

Using the scaling (16), Poiseuille's law (11) becomes

$$\bar{\Psi} = -g(\lambda; \mathcal{K}) \frac{\bar{\Omega}^3}{\gamma} \frac{\partial \Pi}{\partial \xi}, \tag{27}$$

where

$$g(\lambda; \mathcal{K}) = \frac{\pi^2}{12\bar{\Omega}^3} \int_{-\lambda/2}^{\lambda/2} \Omega^3 d\zeta. \tag{28}$$

The function  $g(\lambda; \mathcal{K})$  is a regular, strictly positive function, which asymptotically tends to zero as  $\lambda \rightarrow \infty$ , and  $\lim_{\lambda \rightarrow 1^+} g(\lambda; \mathcal{K}) = 1$ ; however, it cannot be expressed in a closed form. (Details about the asymptotics of the function  $g(\lambda; \mathcal{K})$  can be found in Appendix B.)

It is advantageous to express (27) as

$$\bar{\Psi} = -\frac{1}{\gamma} \Phi(\lambda; \mathcal{K}) \bar{\Omega}^3 \frac{\partial \bar{\Omega}}{\partial \xi}, \tag{29}$$

by defining the shape function  $\Phi$  as

$$\Phi(\lambda; \mathcal{K}) = g \frac{\partial \Pi}{\partial \lambda} \frac{\partial \lambda}{\partial \bar{\Omega}}. \tag{30}$$

Using (19) and (23), the function  $\Phi$  can be written as

$$\Phi(\lambda; \mathcal{K}) = \frac{4\sqrt{\lambda} - \mathcal{K}\sqrt{\lambda^2 - 1}}{\lambda^2(4\sqrt{\lambda} + 3\mathcal{K}\sqrt{\lambda^2 - 1})} g(\lambda; \mathcal{K}). \tag{31}$$

As expected,  $\lim_{\lambda \rightarrow 1^+} \Phi(\lambda; \mathcal{K}) = 1$ . Notice that for  $\mathcal{K} = 0$ , the above expression reduces to

$$\Phi(\lambda; 0) = \lambda^{-2} g(\lambda; 0). \tag{32}$$

The function  $\Phi(\lambda; \mathcal{K})$  eventually becomes negative as  $\lambda$  increases, except for  $\mathcal{K} = 0$  when it tends monotonically to zero. It can readily be shown that the function becomes negative when  $\lambda \geq \lambda_u$ ; indeed both  $\partial \lambda / \partial \bar{\Omega}$  and  $g$  are strictly positive for  $\lambda > 1$  and thus the change of sign in  $\Phi$  simply reflects the change of sign in  $\partial \Pi / \partial \lambda$ , associated with the maximum value of  $\Pi$  achieved at  $\lambda_u$ . A negative value for  $\Phi$  actually implies a reversal of the direction of flow (i.e., the fluid would flow from the tip to the inlet—which is unphysical for a growing fracture) in that part of the fracture for which  $\lambda > \lambda_u$ , unless the gradient of opening  $\partial \Omega / \partial \xi$  also reverses sign, at least locally. This unphysical situation for  $\lambda > \lambda_u$  clearly demonstrates the limitation of the equilibrium height P3D model.

Finally the local continuity equation can be written as

$$\frac{1}{\gamma} \frac{\partial \bar{\Psi}}{\partial \xi} + \bar{\Omega} - \xi \frac{\dot{\gamma}}{\gamma} \frac{\partial \bar{\Omega}}{\partial \xi} + \frac{c}{\sqrt{\tau(1-\theta)}} = 0, \tag{33}$$

where  $\theta(\xi, \tau) = t_0/t$  is the normalized arrival time. Note that the presence of the advective term is due to the stretching nature of the  $\xi$ -coordinate.

### 3.5. Scaled mathematical model

As a result of the above considerations, it is now possible to formulate the P3D model as a non-linear convection diffusion equation for the mean aperture field  $\bar{\Omega}(\xi, \tau)$  and an evolution equation for the fracture length  $\gamma(\tau)$ .

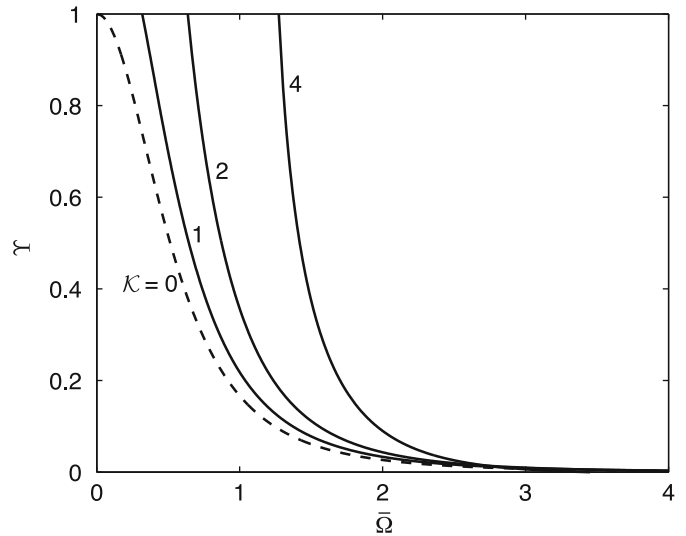


Fig. 4. Plot of function  $\gamma(\bar{\Omega}; \mathcal{K})$  for different values of dimensionless toughness  $\mathcal{K}$ . The dashed line corresponds to  $\mathcal{K} = 0$ .

The governing equation for  $\bar{\Omega}(\xi, \tau)$  is obtained by combining Poiseuille's law (29) and the balance law (33)

$$\bar{\Omega} = \xi \frac{\dot{\gamma}}{\gamma} \frac{\partial \bar{\Omega}}{\partial \xi} + \frac{1}{\gamma^2} \frac{\partial}{\partial \xi} \left( \gamma(\bar{\Omega}; \mathcal{K}) \bar{\Omega}^3 \frac{\partial \bar{\Omega}}{\partial \xi} \right) - \frac{c}{\sqrt{\tau(1-\theta)}}, \tag{34}$$

where the function  $\gamma(\bar{\Omega}; \mathcal{K})$  is defined as

$$\gamma = \Phi(\tilde{\lambda}(\bar{\Omega}), \mathcal{K}), \tag{35}$$

with  $\tilde{\lambda}(\bar{\Omega})$  denoting the inverse function of (23), the relationship between  $\bar{\Omega}$  and the equilibrium height  $\lambda$ . Plots of the function  $\gamma(\bar{\Omega}; \mathcal{K})$  for different values of the dimensionless toughness  $\mathcal{K}$  are shown in Fig. 4. The function  $\gamma(\bar{\Omega}; \mathcal{K})$  is not known in closed form; however, for large  $\bar{\Omega}$ ,  $\gamma \sim \bar{\Omega}^{-4}$  if  $\mathcal{K} = 0$  and  $\gamma \sim \bar{\Omega}^{-8/3}$  if  $\mathcal{K} > 0$ , and

$$\gamma = 1 \quad \text{if } 0 \leq \bar{\Omega} \leq \bar{\Omega}_b, \tag{36}$$

where  $\bar{\Omega}_b$  is the critical value of the aperture at which height growth starts. It is readily deduced from the equilibrium condition (23) between  $\lambda$  and  $\bar{\Omega}$ , which is only valid for  $\lambda > 1$  that  $\bar{\Omega}_b = \mathcal{K}/\pi$ .

Next, an equation for  $\gamma(\tau)$  is obtained by integrating (12) in space over the length of the fracture and then in time from the initial time to the current time to obtain

$$\tau = \gamma \int_0^1 \bar{\Omega}(\xi, \tau) d\xi + 2C\gamma \int_0^1 \sqrt{\tau - \tau_0(\gamma\xi)} d\xi. \tag{38}$$

The boundary conditions at the inlet ( $\xi = 0$ ) and at the leading edge ( $\xi = 1$ ) are given by

$$\bar{\Psi}(0, \tau) = 1, \quad \bar{\Omega}(1, \tau) = \bar{\Psi}(1, \tau) = 0, \quad \tau > 0. \tag{39}$$

Naturally, the boundary conditions in the terms of the flux  $\bar{\Psi}$  can be transformed to be expressed in terms of  $\bar{\Omega}$  only, using (23) and (29).

The initial condition for  $\bar{\Omega}(\xi, \tau)$  is taken to correspond to a small time asymptotic solution when the fracture remains contained in the reservoir layer (i.e.  $\bar{\Omega} \leq \bar{\Omega}_b$ ), and when leak-off is negligible. This similarity solution, referred to as the M-solution below, is governed by (34) with  $\gamma = 1$  and  $c = 0$ .

The system of equations (34), (38), (39), together with the small time asymptotic solution, constitute a closed system to solve for the aperture field  $\bar{\Omega}(\xi, \tau)$  and the fracture length  $\gamma(\tau)$ .

### 3.6. Tip asymptotics

We now examine the nature of the solution near the leading edge. In the neighbourhood of the tip, the leak-off term  $C/\sqrt{\tau(1-\theta)}$  can be approximated as

$$\frac{C}{\sqrt{\tau(1-\theta)}} \simeq C\sqrt{\frac{\dot{\gamma}}{\gamma(1-\xi)}}, \quad 1-\xi \ll 1. \quad (40)$$

Using (40), the balance equation (33) is integrated in a small region of size  $\varepsilon \ll 1$  near the leading edge

$$\int_{1-\varepsilon}^1 \left[ \frac{1}{\gamma} \frac{\partial \bar{\Psi}}{\partial \xi} + \bar{\Omega} - \xi \frac{\dot{\gamma}}{\gamma} \frac{\partial \bar{\Omega}}{\partial \xi} + C \left( \frac{\dot{\gamma}}{\gamma(1-\xi)} \right)^{1/2} \right] d\xi = 0, \quad (41)$$

which, after taking into account the boundary conditions  $\bar{\Psi} = \bar{\Omega} = 0$  at  $\xi = 1$ , implies that

$$\bar{\Psi}^{\xi \rightarrow 1} \sim \dot{\gamma} \bar{\Omega} + 2C\sqrt{\gamma \dot{\gamma} (1-\xi)}. \quad (42)$$

Combining (42) with Poiseuille's law (29) then yields

$$\frac{\bar{\Omega}^3}{\gamma} \frac{\partial \bar{\Omega}}{\partial \xi} + \dot{\gamma} \bar{\Omega} + 2C\sqrt{\gamma \dot{\gamma} (1-\xi)}^{\xi \rightarrow 1} \simeq 0, \quad (43)$$

where we have taken into account that  $\Phi \sim 1$  as  $\xi \rightarrow 1$ .

In the two limiting cases of storage- and leak-off-dominated asymptotics, the behaviour of  $\bar{\Omega}$  near the leading edge can be deduced from (43), by adopting an asymptotic solution for  $\bar{\Omega}$  of the form

$$\bar{\Omega}^{\xi \rightarrow 1} \simeq A(\tau)(1-\xi)^\alpha. \quad (44)$$

In the storage-dominated case, the first two terms in (43) have to balance; hence

$$\alpha = \frac{1}{3}, \quad A = \sqrt[3]{3\dot{\gamma}\gamma}. \quad (45)$$

In the leak-off-dominated case, however, the first and third term in (43) have to balance; hence the power law index  $\alpha$  and the strength  $A$  are given by

$$\alpha = \frac{3}{8}, \quad A = \frac{2}{3^{1/4}} (\dot{\gamma}\gamma^3 C^2)^{1/8}. \quad (46)$$

The tip asymptotic behaviour in between these two limiting cases can also be obtained, see [30] for more details. However, a pragmatic approach is to adopt (45) when  $\gamma < \gamma_c$  (or  $\tau < \tau_c$ ) and (46) when  $\gamma \geq \gamma_c$  (or  $\tau \geq \tau_c$ ) where

$$\gamma_c = \frac{\gamma_{m0}^{8/3}}{\gamma_{m0}^{5/3}} \tau_c = \left( \frac{\gamma_{m0}}{\gamma_{m0}(C)} \right)^{10/3}, \quad (47)$$

with  $\gamma_{m0}$  and  $\gamma_{m0}(C)$ , two numbers that are related to the asymptotics of the fracture length for a PKN fracture at small and large time, i.e. when the contained fracture propagates in the storage- and leak-off-dominated regime, respectively (see (48) and (49)). The length  $\gamma_c$  corresponds to the intersection of the small and large time asymptotic solutions for the length of a PKN fracture, while  $\tau_c$  is the time corresponding to the intersection of these two asymptotes. In the MATLAB code *colP3D* [31] that implements the algorithm presented in this paper, the switch between the two tip asymptotes is based on the time criterion. This approach (based on either the length or the time criterion) is empirically justified by the observations, reported further in this paper, that the evolution of the fracture length is influenced little by the height growth. An alternative empirical approach would be to switch from (45) to (46) for the tip asymptote, when the tip velocity decreases below a critical value deduced from comparing the small and large time asymptotics for the tip velocity of a contained fracture.

## 4. Regimes of solution

### 4.1. Time scales and similarity solutions

The P3D fracture problem is governed by two time scales, one legislating the height growth and the other characterizing the transition from a storage-dominated to a leak-off-dominated regime.

The characteristic time  $t_*$  introduced earlier does not depend on the toughness  $K_{Ic}$  of the adjacent layers, nor on the leak-off coefficient  $C'$  of the reservoir layer. It actually represents the time scale needed to reach, under the particular conditions  $C = \mathcal{K} = 0$ , a large time similarity solution characterized by  $\gamma = \text{Const.}$  and  $\bar{\Omega} \sim \tau$  on account that  $\gamma \sim \bar{\Omega}^{-4}$  when  $\tau \gg 1$ . Unfortunately, this similarity solution violates the basic assumption on which the P3D model is based, namely that the flow is mainly horizontal (i.e. longitudinal), and is therefore only a mathematical curiosity devoid of any physical interest. Nonetheless,  $t_*$  represents a scale for the time required to reach this height growth dominated similarity solution.

Under conditions when the fracture remains confined to the reservoir ( $\lambda = 1$ ), the time scale  $C^{-10/3} t_*$  characterizes the transition between a regime where the injected fluid is essentially occupying the fracture to a regime where most of the fluid leaks into the reservoir. Both regimes are described by similarity solutions with a power law dependence on time [30], see Appendix A for further details.

*The M-solution (storage-dominated regime):*

$$\bar{\Omega}(\xi, \tau) = \bar{\Omega}_{m0}(\xi) \tau^{1/5}, \quad \gamma(\tau) = \gamma_{m0} \tau^{4/5}, \quad (48)$$

with  $\gamma_{m0} \simeq 1.006$  and  $\bar{\Omega}_{m0}(0) \simeq 1.326$ .

*The M̄-solution (leak-off-dominated regime):*

$$\bar{\Omega}(\xi, \tau) = \bar{\Omega}_{\bar{m}0}(\xi, C) \tau^{1/8}, \quad \gamma(\tau) = \gamma_{\bar{m}0}(C) \tau^{1/2}, \quad (49)$$

with  $\gamma_{\bar{m}0} = 2/\pi C$  and  $\bar{\Omega}_{\bar{m}0}(0) = 2/\pi^{1/2} C^{1/4}$ .

Thus the transition between the early-time M-solution and the large-time M̄-solution evolves with the dimensionless time  $C^{10/3} \tau$ . Calculations with the PKN model show, with an error of about 2% or less, that the confined fracture grows in the storage-dominated regime if  $C^{10/3} \tau \lesssim 10^{-5}$  and in the leak-off-dominated regime if  $C^{10/3} \tau \gtrsim 10^3$  [30]. Reaching the M̄-solution requires  $\mathcal{K}$  to be large enough (actually at least of order  $O(10C^{-2/3})$ ) to ensure containment of the fracture within the reservoir layer.

The M-solution is of particular importance because it serves as a small time asymptotic solution from which the P3D fracture evolves. While other processes may have taken place at times prior to those at which the M-solution is applicable (for example, when the fracture length is smaller than or of the same order as the reservoir thickness  $H$ ), the existence of an intermediate time similarity solution usually implies that the details of the earlier fracture evolution do not affect the process anymore once the similarity solution develops [32]. This means that the evolution of the P3D fracture can effectively start from the M-solution, and that the prior history can be ignored. However, as shown below, the M-solution is an appropriate small time asymptotic solution for the P3D fracture, only if the dimensionless toughness  $\mathcal{K} > 0$ .

### 4.2. Phases in fracture height growth

In principle, we can identify four phases of height growth during propagation of the P3D hydraulic fracture, which are delimited by three time markers: (i) the breakthrough time  $\tau_b$  corresponding to the onset of height growth, (ii)  $\tau_p$  when the fracture has penetrated into the layers bounding the reservoir

layers throughout its length, and (iii)  $\tau_u$  when height growth becomes unstable.

**Phase 1: Complete fracture containment** ( $\lambda(\xi, \tau) = 1$  for  $0 \leq \xi \leq 1$  and  $\tau \leq \tau_b(C, \mathcal{K})$ ). The fracture opening  $\bar{\Omega}$  is everywhere less than the threshold value  $\bar{\Omega}_b = \mathcal{K}/\pi$  given by (37). During this phase, the fracture behaves according to the PKN solution [9,30].

**Phase 2: Partial fracture containment** ( $\lambda(\xi, \tau) > 1$  for  $0 \leq \xi < \xi_l(\tau)$  and  $\lambda(\xi, \tau) = 1$  for  $\xi_l(\tau) \leq \xi \leq 1$ ;  $\tau_b(C, \mathcal{K}) \leq \tau \leq \tau_p(C, \mathcal{K})$ ). At the interface,  $\bar{\Omega}(\xi_l, \tau) = \bar{\Omega}_b$  and  $\lambda(\xi_l, \tau) = 1$ . The position  $\xi_l(\tau)$  of the interface between the contained and uncontained fracture regions increases with time, with  $\xi_l(\tau_b) = 0$  and  $\xi_l(\tau_p) = 1$ . In the limit  $\mathcal{K} = 0$ , the fracture is never contained, i.e.  $\tau_b = \tau_p = 0$ .

**Phase 3: No fracture containment** ( $\lambda(\xi, \tau) > 1$  for  $0 \leq \xi < 1$  and  $\tau_p(C, \mathcal{K}) \leq \tau \leq \tau_u(C, \mathcal{K})$ ). The fracture opening  $\bar{\Omega}$  is larger than  $\bar{\Omega}_b(C, \mathcal{K})$  throughout  $0 \leq \xi \leq \xi_l(\tau)$  but less than  $\bar{\Omega}_u(C, \mathcal{K})$  at which value the height growth becomes unstable.

**Phase 4: Unstable height growth** ( $\lambda(1, \tau) > \lambda_u(C, \mathcal{K})$  for  $\tau \geq \tau_u(C, \mathcal{K})$ ). The solution loses its physical meaning once the height growth becomes unstable, which corresponds to the condition  $\bar{\Omega} = \bar{\Omega}_u$ , given by

$$\bar{\Omega}_u = \frac{1}{\pi \mathcal{K}^2} \left( 16 + \sqrt{\mathcal{K}^4 + 64} \right) \sqrt{8 + \sqrt{\mathcal{K}^4 + 64}}. \quad (50)$$

Since  $\bar{\Omega}$  is a monotonically decreasing function, i.e.,  $\partial \bar{\Omega} / \partial \xi < 0$  of  $\xi$  (otherwise the fluid flow would be reversed), the runaway condition will first be reached at the inlet. Hence the time  $\tau_u$  at which the instability takes place corresponds to  $\bar{\Omega}(0, \tau_u) = \bar{\Omega}_u$ . The onset of unstable height growth marks the end of applicability of the equilibrium height P3D model, but the beginning of relevance of the dynamic height model.

Unlike the calculations of  $\tau_p$  and  $\tau_u$ , which require solving the full set of equations governing the evolution of the P3D fracture, the breakthrough time  $\tau_b(C, \mathcal{K})$  can be readily calculated from the known contained (PKN) fracture solution. The evolution of the fracture aperture at the wellbore  $\bar{\Omega}_0(\tau) = \bar{\Omega}(0, \tau)$  can be deduced from the PKN solution to be of the form [30]

$$\bar{\Omega}_0(\tau; C, \mathcal{K}) = \left( \frac{2}{C} \right)^{2/3} \bar{\Omega}_{0*} \left( \frac{C^{10/3} \tau}{2^{4/3}} \right), \quad (51)$$

where the function  $\bar{\Omega}_{0*}(\tau_*)$  is the inlet opening in the PKN scaling [30]. Since the fracture starts to grow into the confining layers when the mean fracture aperture at the borehole reaches the threshold  $\bar{\Omega}_b(C, \mathcal{K})$ , the breakthrough time  $\tau_b$  is deduced to be given by

$$\tau_b = \frac{2^{4/3}}{C^{10/3}} \bar{\Omega}_{0*}^{-1} \left( \frac{C^{2/3} \mathcal{K}}{2^{2/3} \pi} \right) \quad (52)$$

where  $\bar{\Omega}_{0*}^{-1}$  denotes the inverse function of  $\bar{\Omega}_{0*}$ . From the known small and large time asymptotics of  $\bar{\Omega}_{0*}$ , the asymptotics of  $\tau_b$  for small and large  $C^{2/3} \mathcal{K}$  can readily be deduced.

**Storage-dominated asymptote:**

$$\tau_{bs} = \left( \frac{\mathcal{K}}{\pi \bar{\Omega}_{m0}(0)} \right)^5 \simeq 0.79710^{-3} \mathcal{K}^5, \quad C^{2/3} \mathcal{K} \lesssim 0.66. \quad (53)$$

**Leak-off-dominated asymptote:**

$$\tau_{bl} = \frac{C^2 \mathcal{K}^8}{2^8 \pi^4}, \quad C^{2/3} \mathcal{K} \gtrsim 8.5 \quad (54)$$

The above expression for  $\tau_{bs}$  shows that the M-solution is not the appropriate early-time solution for the P3D geometry, if  $\mathcal{K} = 0$ . However, we still use the M-solution to initialize the calculations in that case since the correct early time solution has not yet been established.

Contour plots of the breakthrough time  $\tau_b(C, \mathcal{K})$  in the space  $(C, \mathcal{K})$  are shown in Fig. 5.

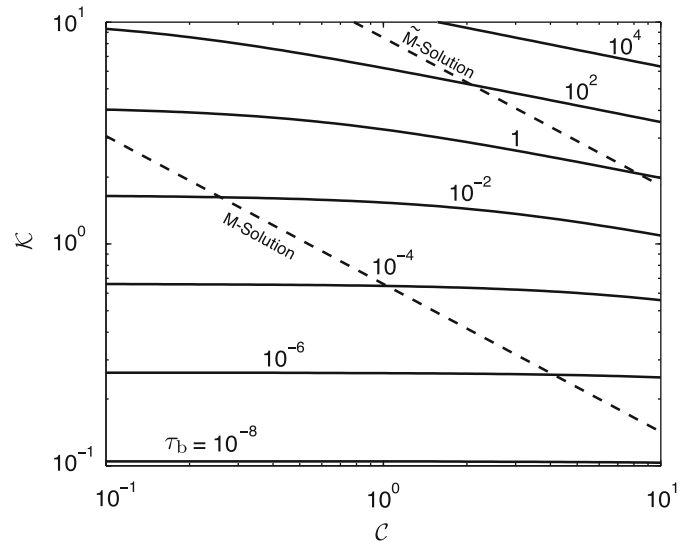


Fig. 5. Contour lines of the breakthrough time  $\tau_b$  in the  $(C, \mathcal{K})$  space.

## 5. Numerical algorithm

### 5.1. A fourth order collocation scheme to solve the model equations

In this section we describe a fourth order collocation scheme to solve the two-point boundary value problem (34) along with the boundary conditions (39). In order to express the model equations as a first order system over the domain  $\xi \in (0, 1)$ , we revert to Poiseuille's law and the original conservation law, which can be expressed in the form

$$\frac{\partial \bar{\Omega}}{\partial \xi} = - \frac{\gamma \bar{\Psi}}{\mathcal{K}(\bar{\Omega}; \mathcal{K}) \bar{\Omega}^3} = F_1(\xi; \bar{\Omega}, \bar{\Psi}, \gamma), \quad (55)$$

$$\frac{\partial \bar{\Psi}}{\partial \xi} = - \frac{\xi \gamma \bar{\Psi}}{\mathcal{K}(\bar{\Omega}; \mathcal{K}) \bar{\Omega}^3} - \gamma \dot{\bar{\Omega}} - \frac{C}{\sqrt{\tau - \tau_0(\gamma \xi)}} = F_2(\xi; \bar{\Omega}, \bar{\Psi}, \gamma). \quad (56)$$

Eq. (38) for  $\gamma(\tau)$ , expressing global conservation of the fracturing fluid, i.e.,

$$\tau = \gamma \int_0^1 \bar{\Omega}(\xi, \tau) d\xi + 2C\gamma \int_0^1 \sqrt{\tau - \tau_0(\gamma \xi)} d\xi \quad (57)$$

completes the system of equations. The time derivatives in (55) and (56) are replaced by the following backward difference approximations:

$$\dot{\gamma} \simeq \frac{\gamma_\tau - \gamma_{\tau - \Delta\tau}}{\Delta\tau} \quad \text{and} \quad \dot{\bar{\Omega}} \simeq \frac{\bar{\Omega}_\tau - \bar{\Omega}_{\tau - \Delta\tau}}{\Delta\tau}. \quad (58)$$

With these difference approximations, (55) and (56) are reduced to a system of ordinary differential equations for  $\bar{\Omega}$  and  $\bar{\Psi}$ , which, when combined with (57), form a nonlinear system that is sufficient to determine  $(\bar{\Omega}, \bar{\Psi}, \gamma)$  at time  $\tau$  given the values at  $\tau - \Delta\tau$ . This time stepping strategy can be interpreted as the backward Euler approximation to the time derivatives in a method of lines scheme in which the spatial discretization has yet to be defined. The inlet boundary condition  $\bar{\Psi}(0, \tau) = 1$  is imposed at the left endpoint of the domain. At the right endpoint of the domain  $\xi = 1$ , corresponding to the fracture tip, we have seen from our asymptotic analysis that  $\bar{\Omega} \sim A(\tau)(1 - \xi)^\alpha$ , where  $0 < \alpha < 1$ . Thus polynomial approximations to  $\bar{\Omega}$ , which include the tip, would be inaccurate due to the fact that the derivatives of  $\bar{\Omega}$  are singular. For this reason we decompose the interval  $[0, 1]$  as follows  $[0, 1] = [0, \xi_c] \cup (\xi_c, 1]$  into a channel region  $[0, \xi_c]$  and a tip region  $(\xi_c, 1]$ . In the channel region we apply a collocation approximation

to (55) and (56) and use a consistent approximation for the integrals in (57). The right boundary condition for this system of ODE is then provided by the appropriate tip asymptotic solution (44) evaluated at  $\xi_c$ , while the remaining contributions from the tip region to the integrals in (57) are determined by the tip asymptotics. In particular, assuming the asymptotic behavior (44) we obtain the following approximation for the storage integral over the tip region:

$$\int_{\xi_c}^1 \bar{\Omega}(\xi, \tau) d\xi \approx \frac{A(\tau)}{1+\alpha} (1-\xi_c)^{1+\alpha} \quad (59)$$

and we make the following approximation to the leak-off integral over the tip region:

$$\int_{\xi_c}^1 \sqrt{\tau-\tau_0}(\gamma\xi) d\xi \approx \int_{\xi_c}^1 \sqrt{\frac{\gamma}{\gamma}}(1-\xi) d\xi = \left(\frac{\gamma}{\gamma}\right)^{1/2} \frac{2}{3} (1-\xi_c)^{3/2}. \quad (60)$$

In order to discretize the nonlinear system (55) and (56), the interval  $[0, \xi_c]$  is partitioned into  $n-1$  subintervals with break-points  $\{0 = \xi_1, \xi_2, \dots, \xi_{n-1}, \xi_n = \xi_c\}$ . Defining the vector  $Y = (\bar{\Omega}, \bar{\Psi})$  we can re-write the system of equations (55) and (56) in the following compact form:

$$\frac{dY}{d\xi} = F(\xi; Y, \gamma), \quad (61)$$

where  $\gamma$  is regarded as a parameter and the components of the gradient field  $F(\xi; Y, \gamma)$  are defined in (55) and (56). Following the approximation scheme adopted in [33], we assume a Hermite cubic approximation to  $Y$  on each subinterval. Integrating (61) over a typical subinterval  $[\xi_k, \xi_{k+1}]$ , we obtain an integral form of (61), which we then approximate using Simpson's Rule

$$\begin{aligned} Y_{k+1} &= Y_k + \int_{\xi_k}^{\xi_{k+1}} F(\xi; Y(\xi), \gamma) d\xi \\ &= Y_k + \frac{\Delta\xi}{6} [F_{k+1} + 4F_{k+\frac{1}{2}} + F_k] + O(\Delta\xi^5). \end{aligned}$$

As in [33] we use the following Hermite cubic approximant to  $\bar{Y}_{k+1/2} = (Y_k + Y_{k+1})/2 - (\Delta\xi/8)(F_{k+1} - F_k)$  to evaluate  $F_{k+1/2} \approx F(\xi_{k+1/2}, \bar{Y}_{k+1/2})$  in the Simpson approximation. Consistent with the above approximation, we use the Composite Simpson's Rule to approximate the storage and leak-off integrals over the channel region.

The above discretizations reduce the continuous system (55)–(57) to a system of  $2n-1$  nonlinear equations for the  $2n+1$  unknowns  $\{\bar{\Omega}_1, \dots, \bar{\Omega}_n; \bar{\Psi}_1, \dots, \bar{\Psi}_n; \gamma\}$ . The two boundary conditions  $\bar{\Psi}_1 = 1$  and  $\bar{\Omega}_n = \bar{\Omega}_{tip}(\xi_c)$  provide the additional constraints required to solve for the  $2n+1$  unknowns. The complete system of nonlinear equations is solved at each time step using a Newton iteration scheme in which a finite difference approximation is used to evaluate the Jacobian for the system at each iteration.

### 5.2. Accuracy and robustness of the algorithm

The spatial discretization used in the numerical scheme has a global truncation error of  $O(\Delta\xi^4)$ , see [33], while the backward difference formula used to approximate the time derivatives has a truncation error of  $O(\Delta\tau)$ . To match the spatial to time scaling  $\xi/\sqrt{\tau}$ , which is intrinsic to diffusion problems, it might be desirable to use a second order backward difference approximation to achieve a truncation order  $O(\Delta\xi^4, \Delta\tau^2)$ . However, we have chosen not to do this in order to maintain the simplicity and brevity of the code which can be downloaded [31]. For this class of problems an explicit time stepping scheme would require a CFL condition of the form  $\Delta\tau \leq k\Delta\xi^2$ , necessitating extremely small time steps and long run times. Since the implicit backward difference time stepping scheme used in this algorithm is an L-stable method there is no time step restriction. In order to

perform simulations that connect both small and large time scales, we have found that increasing the size of the time step by a geometric factor  $r > 1$ , i.e.,  $\Delta\tau_{k+1} = r\Delta\tau_k$  at each time step to be a successful approach. For the results presented in the next section, we have chosen a conservative approach for the choice of the geometric time factor  $r=1.01$  in order to reduce the  $O(\Delta\tau)$  truncation errors to a minimum. For the problems in which we explore the penetration of the layers, we have also chosen a relatively fine spatial mesh  $n=60$  in order to be able to capture the evolving penetration boundary  $\lambda = 1$  with greater resolution. However, substantially larger  $r > 2$  factors are possible without adversely affecting the results and, as the comparisons with the PKN asymptotic solutions demonstrate, a coarse mesh comprising just  $n=10$  collocation points yields results that are almost indistinguishable from the asymptotic solutions.

## 6. Numerical simulations

In this section, we report results of a series of numerical simulations carried out with the MATLAB code *colP3D* [31] that implements the algorithm described above. First, we validate the algorithm by comparing the results of the simulations with the known small and large time asymptotic solutions under conditions when height growth is prohibited. Second, we perform a series of simulations in which height growth is allowed and for which the leak-off and toughness parameters,  $C$  and  $\mathcal{K}$ , assume one of the values 0 or 1.

### 6.1. Simulation without height growth (PKN)

To validate the numerical algorithm, we conducted a simulation by forcing the fracture to remain contained within the reservoir layer (i.e.,  $\lambda(\xi, \tau) = 1$ ), which formally corresponds to the limiting case  $\mathcal{K} = \infty$ . Although the dimensionless leak-off coefficient  $C$  can be absorbed through a rescaling of the equations in this particular case, by redefining the characteristic time, length, and width (see Appendix A), the calculations were nonetheless performed on the basis of the originally scaled equations for  $C = 1$ . The discretization parameters for the simulation were  $n=10$  and  $r=1.2$ . The calculations were started at  $\tau = 10^{-8}$  with an initial time step  $\Delta\tau = 10^{-9}$ , and ended at  $\tau = 10^5$ , so as to guarantee that the computed solution indeed evolves from the small time to the large time similarity solution.

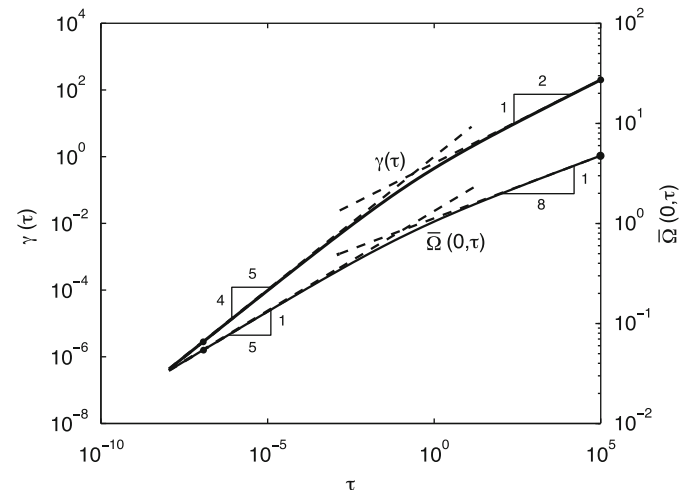


Fig. 6. Comparison between computed  $\gamma(\tau)$  and  $\Omega(0, \tau)$  for imposed  $\lambda = 1$  (PKN solution) with small and large time asymptotics (calculation performed for  $C = 1$ ).

The computed evolution of the fracture length,  $\gamma(\tau)$ , and of the average aperture at the inlet,  $\bar{\Omega}(0,\tau)$ , is shown in Fig. 6, together with the small and large time asymptotes. It can be seen that the computed solution faithfully tracks the small time asymptotics initially and recovers the large time asymptotics very well at the end of the simulation. A comparison between the aperture profile computed at the beginning of the simulation ( $\tau = 1.16 \times 10^{-7}$ ) with that corresponding to the small time similarity solution is shown in Fig. 7. In this figure the solid circles correspond to the actual collocation points whereas the open circles correspond to the midpoint values at which the Hermite cubic interpolants  $\tilde{Y}_{k+1/2}$  are used. The time horizon at which these aperture profiles are sampled is denoted by the first pair of solid circles shown on the fracture length and aperture plots presented in Fig. 6. A similar comparison at the end of the simulation ( $\tau = 10^5$ ) with the large time similarity solution can be found in Fig. 8. The time horizon at which these aperture profiles are sampled is denoted

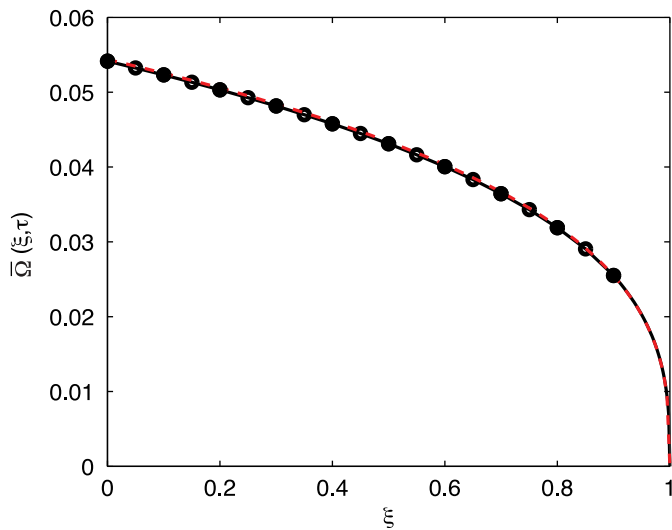


Fig. 7. Comparison between  $\bar{\Omega}(\xi,\tau)$  computed for  $\tau = 1.16 \times 10^{-7}$  and  $C = 1$  (with  $\lambda = 1$ ) and small time similarity solution (shown in red dashed line). (For interpretation of the references to colour in this figure legend, the reader is referred to the web version of this article.)

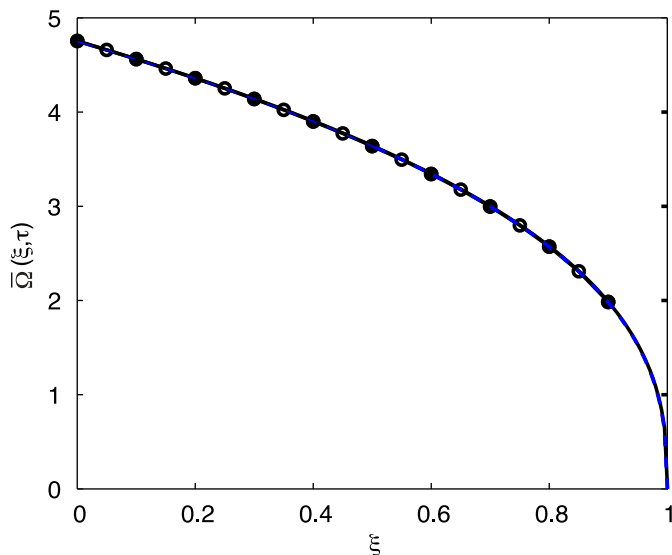


Fig. 8. Comparison between  $\bar{\Omega}(\xi,\tau)$  computed for  $\tau = 10^5$  and  $C = 1$  (with  $\lambda = 1$ ) and large time similarity solution (shown in blue dashed line). (For interpretation of the references to colour in this figure legend, the reader is referred to the web version of this article.)

by the last pair of solid circles shown on the fracture length and aperture plots presented in Fig. 6. The numerical and the closed-form solutions are virtually indistinguishable on both plots.

### 6.2. Simulations with height growth

A series of four simulations with height growth were undertaken with  $C$  and  $\mathcal{K}$ , each taking the values 0 or 1. The discretization parameters for the simulation were  $n=60$  and  $r=1.01$ . We choose to use a large number of spatial collocation points in order to ensure that we capture the penetration free boundary  $\lambda = 1$  with sufficient resolution. In addition, we choose this modest geometric growth factor for the time step to ensure that the truncation error due to the first order time discretization remains negligible. The calculations were started at  $\tau = 10^{-8}$  with an initial time step  $\Delta\tau = 10^{-9}$  for both  $C = 0$  and 1. The simulation proceeded until  $\tau = 10^2$  or  $\lambda(0,\tau) = 5.0$  whichever event occurred first.

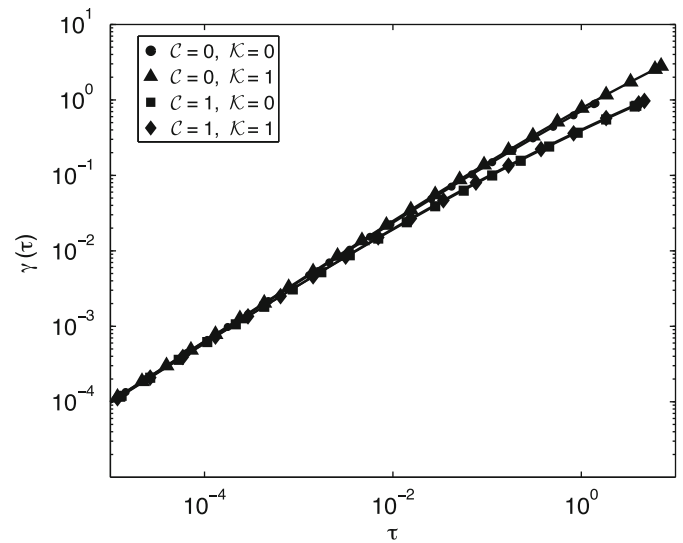


Fig. 9. Plot of the evolution of the length of one fracture wing  $\gamma(\tau)$  for (i)  $C = 0, \mathcal{K} = 0$ , (ii)  $C = 0, \mathcal{K} = 1$ , (iii)  $C = 1, \mathcal{K} = 0$ , and (iv)  $C = 1, \mathcal{K} = 1$ .

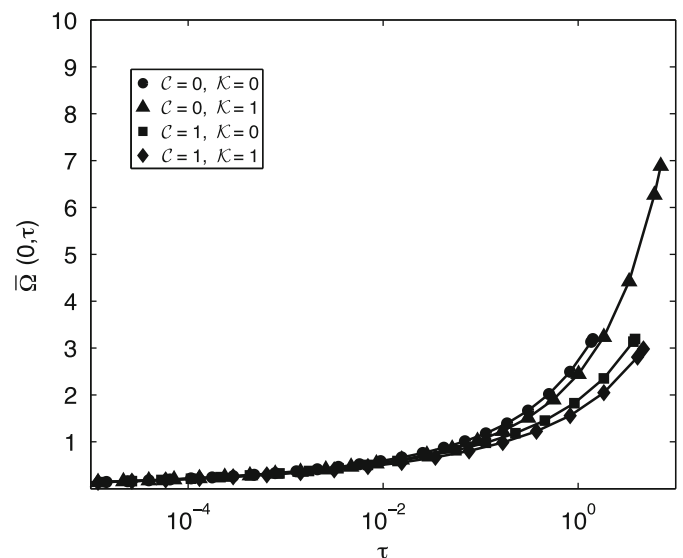


Fig. 10. Plot of the evolution of the inlet average opening  $\bar{\Omega}(0,\tau)$  for (i)  $C = 0, \mathcal{K} = 0$ , (ii)  $C = 0, \mathcal{K} = 1$ , (iii)  $C = 1, \mathcal{K} = 0$ , and (iv)  $C = 1, \mathcal{K} = 1$ .

The evolution of the fracture length,  $\gamma(\tau)$ , the average fracture aperture at the borehole,  $\bar{\Omega}(0,\tau)$ , and the fracture height at the inlet,  $\lambda(0,\tau)$ , are shown in Figs. 9–11. Notwithstanding the use of logarithmic scales for both time and length axes in Fig. 9, it can be seen that the toughness  $\mathcal{K}$  has little influence on the fracture length evolution. As expected, leak-off slows fracture propagation. The variation with time of the average fracture opening at the inlet, shown in Fig. 10, is also not influenced much by  $\mathcal{K}$ . These observations suggest that the treatment efficiency  $\eta$  defined as

$$\eta = \frac{2}{\tau} \int_0^1 \bar{\Omega} d\xi$$

is not sensitive to  $\mathcal{K}$ , as confirmed by Fig. 12. The evolution of the fracture height at the borehole shown in Fig. 11 indicates a strong dependence of  $\lambda$  on both  $C$  and  $\mathcal{K}$ . In particular,  $\mathcal{K}$  delays the onset of the breakthrough into the adjacent layers. Fig. 13 shows the influence of both  $C$  and  $\mathcal{K}$  on the evolution of the inlet net pressure  $\Pi(0,\tau)$ . The larger  $\bar{\Omega}(0,\tau)$  and  $\lambda(0,\tau)$  values associated with  $C=0$

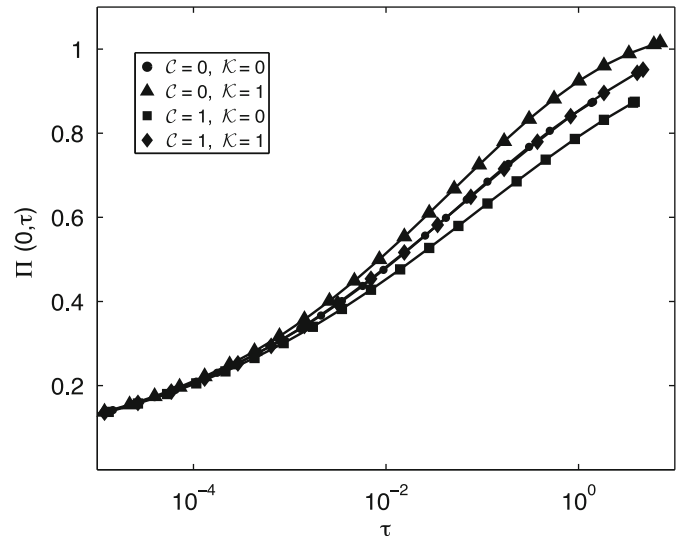


Fig. 13. Plot of the evolution of the inlet net pressure  $\Pi(0,\tau)$  for (i)  $C=0, \mathcal{K}=0$ , (ii)  $C=0, \mathcal{K}=1$ , (iii)  $C=1, \mathcal{K}=0$ , and (iv)  $C=1, \mathcal{K}=1$ .

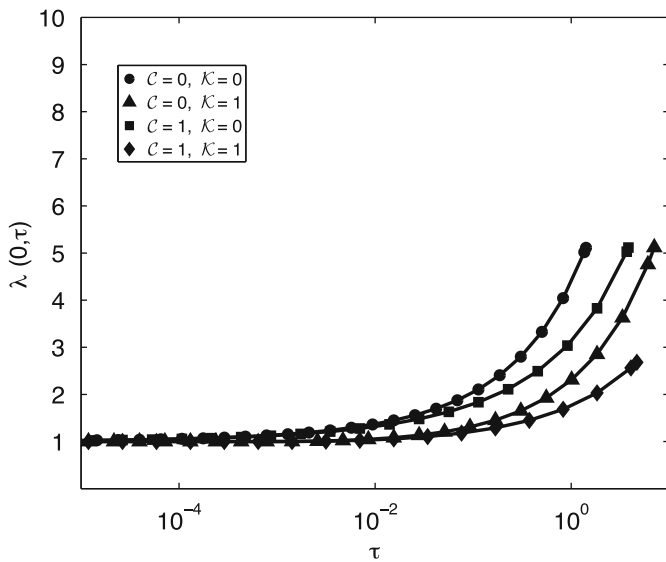


Fig. 11. Plot of the evolution of the inlet fracture height  $\lambda(0,\tau)$  for  $C=0, \mathcal{K}=0$ ,  $C=0, \mathcal{K}=1$ ,  $C=1, \mathcal{K}=0$ ,  $C=1, \mathcal{K}=1$ .

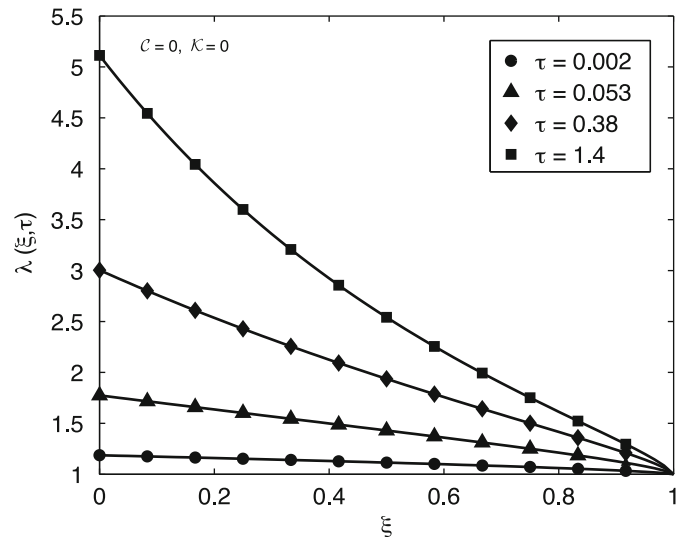


Fig. 14. Fracture height profile  $\lambda(\xi,\tau)$  for selected  $\tau$  and  $C=0, \mathcal{K}=0$ .

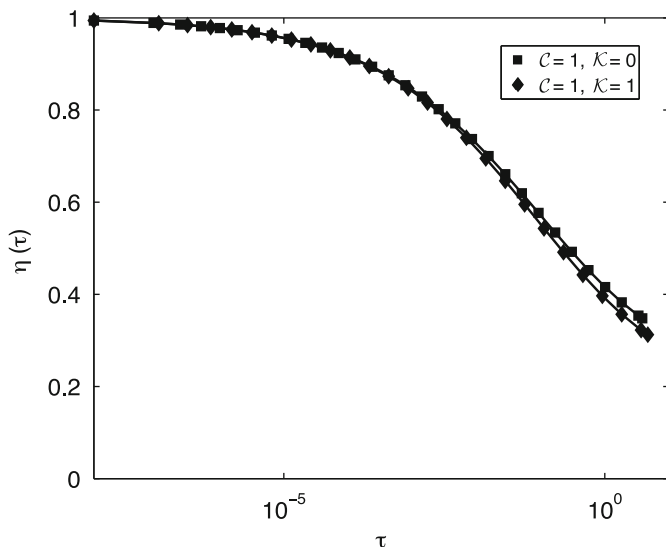


Fig. 12. Plot of the evolution of the efficiency  $\eta(\tau)$  for (i)  $C=1, \mathcal{K}=0$  and (ii)  $C=1, \mathcal{K}=1$ .

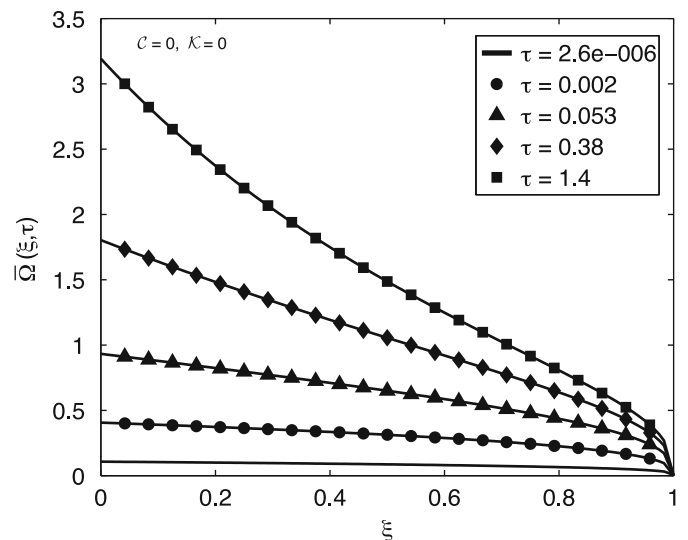


Fig. 15. Average fracture opening profile  $\bar{\Omega}(\xi,\tau)$  for selected  $\tau$  and  $C=0, \mathcal{K}=0$ .

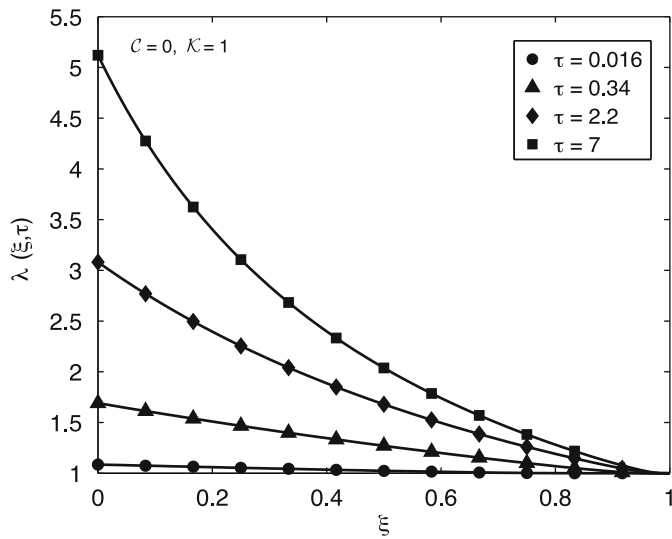


Fig. 16. Fracture height profile  $\lambda(\xi, \tau)$  for selected  $\tau$  and  $C=0, \mathcal{K}=1$ .

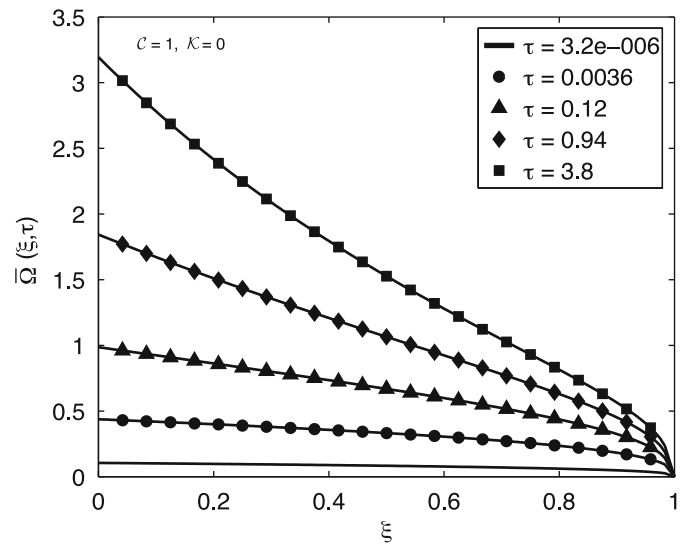


Fig. 19. Average fracture opening profile  $\bar{Q}(\xi, \tau)$  for selected  $\tau$  and  $C=1, \mathcal{K}=0$ .

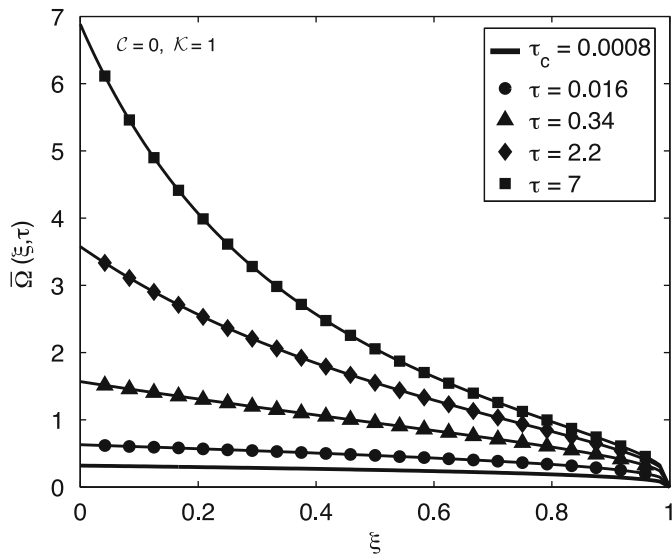


Fig. 17. Average fracture opening profile  $\bar{Q}(\xi, \tau)$  for selected  $\tau$  and  $C=0, \mathcal{K}=1$ .

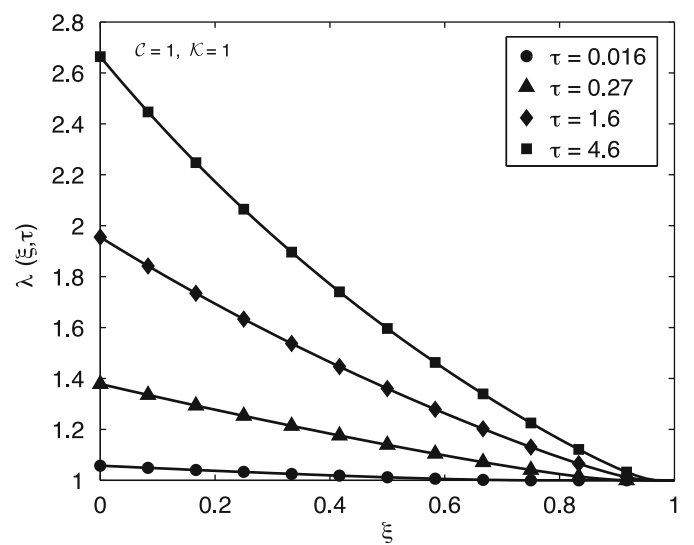


Fig. 20. Fracture height profile  $\lambda(\xi, \tau)$  for selected  $\tau$  and  $C=1, \mathcal{K}=1$ .

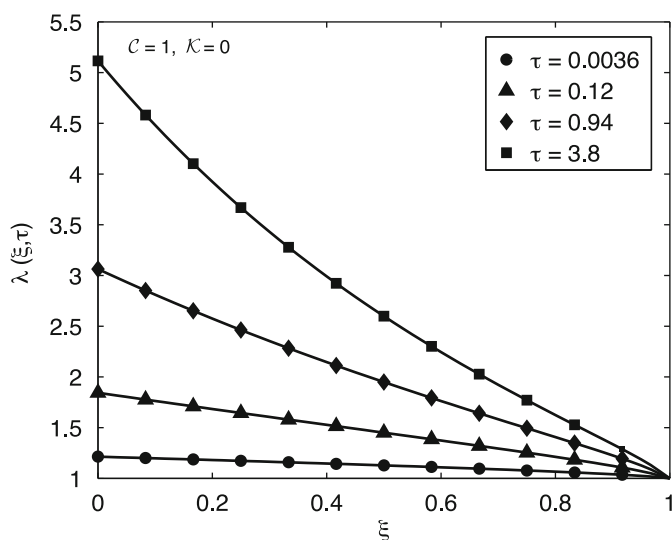


Fig. 18. Fracture height profile  $\lambda(\xi, \tau)$  for selected  $\tau$  and  $C=1, \mathcal{K}=0$ .

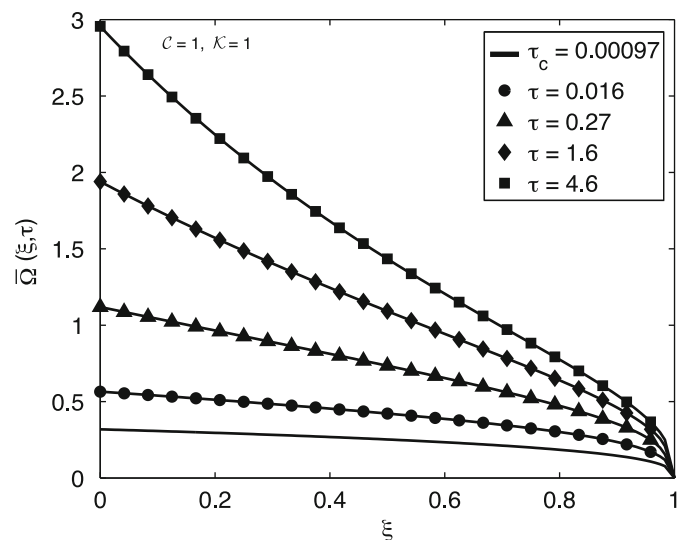


Fig. 21. Average fracture opening profile  $\bar{Q}(\xi, \tau)$  for selected  $\tau$  and  $C=1, \mathcal{K}=1$ .

and  $\mathcal{K}=0$  seem to yield the same  $\Pi(0,\tau)$  values as the much smaller  $\bar{\Omega}(0,\tau)$  and  $\lambda(0,\tau)$  values associated with the case  $\mathcal{C}=1$  and  $\mathcal{K}=1$ . These simulations imply therefore that the fracture length, mean fracture opening, and efficiency are mainly affected by the leak-off coefficient  $\mathcal{C}$ . The toughness  $\mathcal{K}$  essentially impacts the vertical growth of the fracture, the maximum fracture aperture, and the fracture pressure.

Figs. 14–21 display the fracture height profile  $\lambda(\xi,\tau)$  and opening profile  $\bar{\Omega}(\xi,\tau)$  at selected times for the four cases considered. The opening profiles at the time of breakthrough,  $\tau_b$ , for  $\mathcal{K}=1$  (or at the start of the simulation for  $\mathcal{K}=0$ ) are represented by continuous lines without symbols in these figures. These profiles demonstrate the dramatic influence of the fracture height growth on the shape of the fracture opening profile.

## 7. Conclusions

In this paper we have revisited the classical equilibrium height “Pseudo-3D” model of a hydraulic fracture, which is used in the design of most hydraulic fracturing treatments. This model, introduced in the early 1980s by a number of researchers as an extension of the PKN model, allows for penetration of the fracture into the layers bounding the hydrocarbon reservoirs, while maintaining all the other simplifying assumptions on which the PKN model is built. The paper takes a different tack from previous contributions on the P3D model. Rather than following *ab initio* a discrete formalism, it first adopts a continuous formulation and scaling of the problem, thus allowing for further analysis of the mathematical model before embarking on the development of a numerical algorithm. This approach leads to a nonlinear convection diffusion equation with a delay term that governs the mean fracture aperture  $\bar{\Omega}$ , supplemented by an integral condition to be solved for the fracture length  $\gamma$ .

In this novel formulation of the P3D model, the effect of the height growth is entirely embodied in the function  $\gamma(\bar{\Omega})$ —a source of additional non-linearity in the P3D model compared with the PKN model, as this function is simply unity if the fracture remains confined to the reservoir. The function  $\gamma(\bar{\Omega})$  captures the variation of the hydraulic conductivity associated with penetration of the fracture into the adjacent layers, while implicitly accounting for the propagation criterion that controls its vertical growth. Although the paper restricts consideration to the simple but important case of identical elastic properties for the reservoir, with impermeable bounding layers and symmetric stress barriers, the formulation used is general. Other factors influencing fracture height growth, such as multiple bounding layers with different elastic properties and confining stresses, can simply be assimilated in the function  $\gamma(\bar{\Omega})$ , which is in principle computable. Even for the simple configuration of concern here, the function  $\gamma(\bar{\Omega})$  is not known in closed form. However, its dependence on one number only, the scaled toughness  $\mathcal{K}$  of the bounding layers, ensures that it can easily be pre-tabulated. Furthermore, the condition of unstable height growth, which marks the limit of validity of one of the key assumptions of the P3D model, namely the vertical uniformity of the fluid pressure, can be determined explicitly in the form of a simple upper bound  $\bar{\Omega}_u(\mathcal{K})$  on  $\bar{\Omega}$ .

Another contribution reported in this paper is the development of an implicit fourth order collocation scheme on a moving mesh to solve the nonlinear partial differential equations and the integral relation governing the response of the P3D model. The numerical method, which approximates both the mean fracture opening  $\bar{\Omega}$  and the mean flux  $\bar{\Psi}$  by a cubic polynomial over a discretization interval, is fourth order accurate in the space variable. Despite being first order accurate in time, a doubling of

the size of the time step at each new step still leads to accurate results while permitting a very rapid simulation over many temporal orders of magnitude. The fourth order spatial approximation numerical scheme implies that the solution could satisfactorily be captured using a rather coarse mesh. However, the accurate tracking of the penetration front ( $\lambda=1$ ) during the propagation phase, when the fracture is partially contained, requires sufficient spatial resolution of the computational grid. Nonetheless, this algorithm could, in principle, be improved by explicitly recognizing the existence of a propagation front, through the introduction of two moving meshes: one for the contained region and one for the uncontained region.

Finally, an analysis of the behavior of the P3D model was conducted through a series of numerical simulations. Actually, an assessment of the overall behavior of the system can readily be made, as only two numbers,  $\mathcal{K}$  and  $\mathcal{C}$ , control the solution—thanks to the assumption of symmetric stress barriers, homogeneous elastic properties, and constant injection rate adopted for this study. In particular, the limits of the four regimes of propagation of a P3D fracture (fully, partially, and not contained to the reservoir layer, as well as unstable height growth) can be expressed simply in terms of time thresholds that only depend on  $\mathcal{K}$  and  $\mathcal{C}$ . Also, as realistic values of the physical parameters typically correspond to values of  $\mathcal{K}$  and  $\mathcal{C}$  within the range [0,1], we reported the results of four simulations conducted for each combination of  $\mathcal{K}$  and  $\mathcal{C}$  taking values of 0 or 1 so as to provide glimpse of expected variation in the response of the system. Remarkably, we found that the mean aperture field  $\bar{\Omega}(\xi,\tau)$  and the fracture length  $\gamma(\tau)$  do not deviate significantly from the prediction of the PKN model. However, since the fracture compliance  $c$  is sensitive to the actual height of the fracture, the net pressure is strongly influenced by penetration of the fracture into the bounding layers.

The rigorous mathematical formulation of the P3D model presented in this paper has made it possible to clearly identify the important regimes of propagation from a contained fracture initiating in the storage regime to a final state comprising a partially or fully penetrated fracture propagating in the leak-off dominated regime. A clear criterion for the onset of runaway height growth, beyond which the model fails to be valid, has also been established. The scaling analysis has made it possible to clearly establish the fundamental relationship between the front propagation dynamics and the propagation regimes of the classical PKN model and the P3D model. The novel implicit spatially fourth order collocation scheme is shown to be robust and makes it possible to accurately explore the behavior of the solution over the large range of time scales active in the problem. The algorithm implemented in the downloadable MATLAB code *colP3D* [31] could in principle be extended to account for power law fluids, proppant transport, variable injection rate and multiple layers. Such extensions would make it a useful design code for Industry.

## Acknowledgements

J.I.A. would like to Schlumberger for permission to publish. E. Detournay gratefully acknowledges support from the National Science Foundation under Grant no. 0600058; however, any opinions, findings, and conclusions or recommendations expressed in this material are those of the authors and do not necessarily reflect the views of the National Science Foundation. Finally, A. Peirce acknowledges the support of the NSERC discovery grants program.

**Appendix A. Similarity solutions for contained (PKN) hydraulic fractures**

The solution of the contained hydraulic fracture is well-known [9,34,30]. The quantities can be scaled in such a way that the solution does not depend on any parameters other than the stretching coordinate  $\xi$  and a dimensionless time  $\tau_*$  [30]. The relationship between the scaled quantities introduced in this paper and those defined by [30] (denoted by an asterisk) are given by

$$\bar{\Omega} = \left(\frac{2}{C}\right)^{2/3} \bar{\Omega}_*, \quad \gamma = \left(\frac{2^5}{C^8}\right)^{1/3} \gamma_*, \quad \tau = \left(\frac{2^4}{C^{10}}\right)^{1/3} \tau_* \tag{A.1}$$

The solution degenerates into a similarity solution at small time (the M-solution) ( $\tau_* \lesssim 10^{-4}$ ) and at large time (the M-solution) ( $\tau_* \gtrsim 10^2$ ), both characterized by a power law dependence on time.

*M-solution.* The small time asymptotic solution behaves with time according to

$$\gamma(\tau) = \gamma_{m0} \tau^{4/5}, \quad \Omega(\xi, \tau) = \Omega_{m0}(\xi) \tau^{1/5}, \quad \tau \ll 1, \tag{A.2}$$

with  $\Omega_{m0}(\xi)$  and  $\gamma_{m0}$  governed by

$$\frac{5}{4\gamma_{m0}^2} \frac{d^2 \bar{\Omega}_{m0}^4}{d\xi^2} + 4\xi \frac{d\bar{\Omega}_{m0}}{d\xi} - \bar{\Omega}_{m0} = 0, \quad 2\gamma_{m0} \int_0^1 \Omega_{m0} d\xi = 1, \quad \Omega_{m0}(1) = 0. \tag{A.3}$$

The solution of (A.3) yields

$$\bar{\Omega}_{m0} = \left(\frac{12}{5}\right)^{1/3} \gamma_{m0}^{2/3} (1-\xi)^{1/3} \left(1 - \frac{1}{96}(1-\xi)\right) + O((1-\xi)^{7/3}), \tag{A.4}$$

and  $\gamma_{m0} \simeq 1.00063$ .

*M-solution.* The large time asymptotic solution behaves with time according to

$$\gamma(\tau) = \gamma_{\dot{m}0} \tau^{1/2}, \quad \Omega(\xi, \tau) = \Omega_{\dot{m}0}(\xi) \tau^{1/8}, \quad \tau \gg 1, \tag{A.5}$$

with  $\Omega_{\dot{m}0}(\xi)$  and  $\gamma_{\dot{m}0}$  governed by

$$\frac{d^2 \bar{\Omega}_{\dot{m}0}^4}{d\xi^2} - \frac{4C\gamma_{\dot{m}0}^4}{\sqrt{1-\xi^2}} = 0, \quad 2C\gamma_{\dot{m}0} \int_0^1 \sqrt{1-\xi^2} d\xi = 1. \tag{A.6}$$

The solution of (A.6) yields

$$\bar{\Omega}_{\dot{m}0}(\xi) = \left(\frac{8}{\pi C}\right)^{1/4} \left(\frac{2}{\pi} \xi \arcsin \xi + \frac{2}{\pi} \sqrt{1-\xi^2} - \xi\right)^{1/4}, \quad \gamma_{\dot{m}0} = \frac{2}{\pi C}. \tag{A.7}$$

The series expansion of  $\bar{\Omega}_{\dot{m}0}(\xi)$  with respect to the tip is given by

$$\bar{\Omega}_{\dot{m}0}(\xi) = \frac{2^{11/8}}{\pi^{1/2}(3C)^{1/4}} (1-\xi)^{3/8} \left(1 + \frac{1}{80}(1-\xi)\right) + O((1-\xi)^{19/8}). \tag{A.8}$$

**Appendix B. Asymptotics of the function  $g(\lambda, \mathcal{K})$**

It is possible to extract some information about the asymptotic behaviors of the function  $g(\lambda, \mathcal{K})$ . We first rewrite the aperture  $\Omega(\xi; \mathcal{K}, \lambda)$  in terms of the space variable  $u = 2\xi/\lambda$ , i.e.  $\tilde{\Omega}(2\xi/\lambda; \mathcal{K}, \lambda) = \Omega(\xi; \mathcal{K}, \lambda)$  and express  $\tilde{\Omega}$  into two contributions, one that is independent of  $\mathcal{K}$  and another one that is proportional to  $\mathcal{K}$ . Furthermore, since the aperture is symmetric with respect to  $u=0$ , we are only concerned here with  $u > 0$

$$\tilde{\Omega} = \tilde{\Omega}_0(u; \lambda) + \mathcal{K} \lambda^{1/2} \tilde{\Omega}_k(u), \quad 0 \leq u \leq 1, \tag{B.1}$$

where

$$\tilde{\Omega}_0 = \frac{8}{\pi^2} [\tilde{\phi}_2(u; \lambda) - u \lambda \tilde{\phi}_1(u; \lambda)], \quad \tilde{\Omega}_k = \frac{4}{\pi^2} \sqrt{1-u^2}, \tag{B.2}$$

with

$$\phi_1(u; \lambda) = \begin{cases} \operatorname{arctanh}\left(\frac{u\sqrt{\lambda^2-1}}{\sqrt{1-u^2}}\right), & 0 \leq u < \frac{1}{\lambda}, \\ \operatorname{arctanh}\left(\frac{\sqrt{1-u^2}}{u\sqrt{\lambda^2-1}}\right), & \frac{1}{\lambda} < u \leq 1, \end{cases}$$

$$\phi_2(u; \lambda) = \begin{cases} \operatorname{arctanh}\left(\frac{\sqrt{\lambda^2-1}}{\lambda\sqrt{1-u^2}}\right), & 0 \leq u < \frac{1}{\lambda}, \\ \operatorname{arctanh}\left(\frac{\lambda\sqrt{1-u^2}}{\sqrt{\lambda^2-1}}\right), & \frac{1}{\lambda} < u \leq 1. \end{cases} \tag{B.3}$$

*B.1. Large penetration asymptote*

Let  $\tilde{\Omega}_{0l}$  denote the asymptotics of  $\tilde{\Omega}_0$  for large penetration of the fracture into the bounding layers, i.e., for  $\lambda \gg 1$ , which is given by

$$\tilde{\Omega}_{0l} = \frac{8}{\pi^2} \left[ -\sqrt{1-u^2} + \frac{1}{2} \ln\left(\frac{1+\sqrt{1-u^2}}{1-\sqrt{1-u^2}}\right) \right], \quad \frac{1}{\lambda} < u \leq 1, \quad \lambda \gg 1. \tag{B.4}$$

Consider now the following two integrals,  $\bar{\Omega}(\lambda, \mathcal{K})$  and  $\Theta(\lambda, \mathcal{K})$ :

$$\bar{\Omega} = 2 \int_0^{\lambda/2} \Omega(\xi) d\xi = \lambda \int_0^1 \tilde{\Omega}(u) du, \tag{B.5}$$

$$\Theta = 2 \int_0^{\lambda/2} \Omega^3(\xi) d\xi = \lambda \int_0^1 \tilde{\Omega}^3(u) du. \tag{B.6}$$

The large penetration asymptotes of these two integrals,  $\bar{\Omega}_l$  and  $\Theta_l$  can then be expressed as

$$\bar{\Omega}_l = \mathcal{K} \lambda^{3/2} \int_0^1 \tilde{\Omega}_k du + \lambda \lim_{\lambda \rightarrow \infty} \int_{1/\lambda}^1 \tilde{\Omega}_{0l} du, \tag{B.7}$$

$$\Theta_l = \mathcal{K}^3 \lambda^{5/2} \int_0^1 \tilde{\Omega}_k^3 du + 3\mathcal{K}^2 \lambda^2 \lim_{\lambda \rightarrow \infty} \int_{1/\lambda}^1 \tilde{\Omega}_k^2 \tilde{\Omega}_{0l} du + 3\mathcal{K} \lambda^{3/2} \lim_{\lambda \rightarrow \infty} \int_{1/\lambda}^1 \tilde{\Omega}_k \tilde{\Omega}_{0l}^2 du + \lambda \lim_{\lambda \rightarrow \infty} \int_{1/\lambda}^1 \tilde{\Omega}_{0l}^3 du. \tag{B.8}$$

All the integrals are thus only numbers, independent of either  $\mathcal{K}$  or  $\lambda$ , which can be computed either exactly or numerically

$$\int_0^1 \tilde{\Omega}_k du = \frac{1}{\pi}, \quad \int_0^1 \tilde{\Omega}_{0l} du = \frac{2}{\pi}, \quad \int_0^1 \tilde{\Omega}_k^3 du = \frac{12}{\pi^5},$$

$$\int_0^1 \tilde{\Omega}_k^2 \tilde{\Omega}_{0l} du = \frac{88}{3\pi^5}, \quad \int_0^1 \tilde{\Omega}_k \tilde{\Omega}_{0l}^2 du = \alpha_{12}, \quad \int_0^1 \tilde{\Omega}_{0l}^3 du = \alpha_3,$$

with  $\alpha_{12} \simeq 0.394028$  and  $\alpha_3 \simeq 2.36427$ .

After some manipulations, we can write the large  $\lambda$  asymptote of  $g$ ,  $g_l = \pi^2 \Theta_l / 12 \bar{\Omega}_l^3$ , as

$$g_l = \frac{3\mathcal{K}^3 \lambda^{3/2} + 22\mathcal{K}^2 \lambda + 3a_1 \mathcal{K} \sqrt{\lambda} + 3a_2}{3\lambda^2 (\mathcal{K} \sqrt{\lambda} + 2)^3}, \tag{B.9}$$

where  $a_1 = \alpha_{12} \pi^5 / 4 \simeq 30.145$  and  $a_2 = \alpha_3 \pi^5 / 12 \simeq 60.293$ .

*B.2. Small penetration asymptote*

Let  $\tilde{\Omega}_{0s}$  denote the asymptotics of  $\tilde{\Omega}_0$  for small penetration of the fracture into the bounding layers, i.e., for  $1-\lambda \ll 1$ , which is

given by

$$\tilde{\Omega}_{0s} = \frac{8\sqrt{2}}{\pi^2} \sqrt{\lambda-1} \left[ \sqrt{1-u^2} + \frac{1}{12}(\lambda-1) \frac{1+7u^2}{\sqrt{1-u^2}} \right], \quad 0 < u \leq \frac{1}{\lambda}, \quad 1-\lambda \ll 1. \tag{B.10}$$

Consider now the following two integrals,  $\bar{\Omega}(\lambda, \kappa)$  and  $\Theta(\lambda, \kappa)$ :

$$\bar{\Omega} = 2 \int_0^{\lambda^{1/2}} \Omega(\zeta) d\zeta = \lambda \int_0^1 \tilde{\Omega}(u) du, \tag{B.11}$$

$$\Theta = 2 \int_0^{\lambda^{1/2}} \Omega^3(\zeta) d\zeta = \lambda \int_0^1 \tilde{\Omega}^3(u) du. \tag{B.12}$$

The small penetration asymptotes of these two integrals,  $\bar{\Omega}_s$  and  $\Theta_s$ , can then be expressed as

$$\bar{\Omega}_s = \kappa \lambda^{3/2} \int_0^1 \tilde{\Omega}_\kappa du + \lambda \lim_{\lambda \rightarrow \infty} \int_0^{1/\lambda} \tilde{\Omega}_{0s} du. \tag{B.13}$$

Hence

$$\bar{\Omega}_s \simeq \frac{\kappa}{\pi} \lambda^{3/2} + \frac{2}{\pi} \lambda \sqrt{2(\lambda-1)} \simeq \frac{2\sqrt{2}}{\pi} \lambda \left( \frac{\kappa}{2} \sqrt{\frac{\lambda}{2} + \sqrt{\lambda-1}} \right). \tag{B.14}$$

To calculate  $\Theta_s$  and in order to remove the non-integrable terms, we approximate  $\tilde{\Omega}_s^3$  as

$$\tilde{\Omega}_s^3 \simeq \frac{2^{10}\sqrt{2}}{\pi^6} \left( \frac{\kappa}{2} \sqrt{\frac{\lambda}{2} + \sqrt{\lambda-1}} \right)^3 \left[ (1-u^2)^{3/2} - \frac{1}{4}(1+7u^2)\sqrt{1-u^2}h(\lambda; \kappa) \right], \tag{B.15}$$

where the function  $h(\lambda, \kappa)$  is defined as

$$h = \frac{(\lambda-1)^{3/2}}{\frac{\kappa}{2} \sqrt{\frac{\lambda}{2} + \sqrt{\lambda-1}}}. \tag{B.16}$$

Hence

$$\Theta_s \simeq \frac{3 \cdot 2^6 \sqrt{2}}{\pi^5} \lambda \left( \frac{\kappa}{2} \sqrt{\frac{\lambda}{2} + \sqrt{\lambda-1}} \right)^3 \left[ 1 - \frac{11}{12} h(\lambda; \kappa) \right], \tag{B.17}$$

and

$$g_s = \frac{1}{\lambda^2} \left[ 1 - \frac{11}{12} h(\lambda; \kappa) \right]. \tag{B.18}$$

### B.3. Large $\lambda$ asymptote

For  $\kappa \gg 1$ , the function  $\Omega_0$  can be neglected in front of  $\kappa \lambda^{1/2} \Omega_\kappa$ ; thus

$$\Omega \simeq \frac{4\kappa}{\pi^2 \sqrt{\lambda}} \sqrt{\lambda^2 - 4\zeta^2}, \tag{B.19}$$

and

$$g \simeq \frac{1}{\lambda^2}, \quad \kappa \gg 1 \tag{B.20}$$

which shows that the large  $\kappa$  asymptotics is independent of  $\kappa$ .

## References

[1] Settari A, Cleary MP. Development and testing of a pseudo-three-dimensional model of hydraulic fracture geometry (p3dh). In: Proceedings of the 6th SPE symposium on reservoir simulation of the Society of Petroleum Engineers, SPE 10505, January–February 1982. p. 185–214.  
 [2] Palmer ID, Carroll HB. Three-dimensional hydraulic fracture propagation in the presence of stress variation. In: Proceedings of the SPE/DOE/GRI unconventional gas recovery symposium, SPE/DOE 10849, May 1982. p. 870–8.  
 [3] Palmer ID, Carroll HB. Numerical solution for height and elongated hydraulic fractures. In: Proceedings of the SPE/DOE low permeability reservoir

symposium, Denver. SPE 11627, Society of Petroleum Engineers, 1983. p. 249–6.  
 [4] Palmer ID, Craig HR. Modeling of asymmetric vertical growth in elongated hydraulic fractures and application to first MWX stimulation. In: Proceedings of the SPE/DOE/GRI unconventional gas recovery symposium, SPE 12879, 1984. p. 453–62.  
 [5] Settari A, Cleary MP. Development and testing of a pseudo-three-dimensional model of hydraulic fracture geometry. SPE Production Engineering, November 1986. p. 449–66.  
 [6] Meyer BR. Design formulae for 2d and 3-d vertical hydraulic fractures: model comparison and parametric studies. In Proceedings of the unconventional gas technology symposium, SPE 15240, 1986. p. 391–408.  
 [7] Mack MG, Warpinski R. Mechanics of hydraulic fracturing. In: Economides MJ, Nolte KG, editors. Reservoir stimulation, 3rd ed.. Chichester, UK: John Wiley & Sons; 2000. [Chapter 6].  
 [8] Perkins TK, Kern LR. Widths of hydraulic fractures. J Pet Tech Trans AIME 1961;222:937–49.  
 [9] Nordgren RP. Propagation of vertical hydraulic fractures. J Pet Technol 1972;253:306–14. (SPE 3009).  
 [10] Clifton RJ, Abou-Sayed AS. On the computation of the three-dimensional geometry of hydraulic fractures. In: Proceedings of the SPE symposium on low permeability gas reservoirs, Denver, Richardson, TX. Society of Petroleum Engineers (SPE 7943); 1979. p. 307–13.  
 [11] Clifton RJ, Abou-Sayed AS. A variational approach to the prediction of the three-dimensional geometry of hydraulic fractures. In: Proceedings of the SPE/DOE Low Permeability Reservoir Symposium, Denver. Richardson, TX: Society of Petroleum Engineers (SPE 9879); 1981.  
 [12] Clifton RJ. Three-dimensional fracture-propagation models. In: Gidley JL, Holditch SA, Nierode DE, Veatch RW, editors. Recent advances in hydraulic fracturing—SPE monographs, vol. 12. Society of Petroleum Engineers; 1989. p. 95–108.  
 [13] Wang JJ, Clifton RJ. Numerical modeling of hydraulic fracturing in layered formations with multiple elastic moduli. In: Rock mechanics contributions and challenges. Rotterdam: Balkema; 1990. p. 303–10.  
 [14] Advani SH, Lee TS, Lee JK. Three dimensional modeling of hydraulic fractures in layered media: finite element formulations. ASME J Energy Res Technol 1990;112:1–18.  
 [15] Peirce AP, Siebrits E. The scaled flexibility matrix method for the efficient solution of boundary value problems in 2D and 3D layered elastic media. Comput Meth Appl Mech Eng 2001;190:5935–56.  
 [16] Peirce AP, Siebrits E. Uniform asymptotic approximations for accurate modeling of cracks in layered elastic media. Int J Fract 2001;110: 205–39.  
 [17] Siebrits E, Peirce AP. An efficient multi-layer planar 3D fracture growth algorithm using a fixed mesh approach. Int J Numer Meth Eng 2002;53: 691–717.  
 [18] Peirce AP, Detournay E. An implicit level set method for modeling hydraulically driven fractures. Comput Meth Appl Mech Eng 2008;197: 2858–85.  
 [19] Adachi JI, Peirce AP. Asymptotic analysis of an elasticity equation for a finger-like hydraulic fracture. J Elasticity 2007;90(1):43–69.  
 [20] Carter ED. Optimum fluid characteristics for fracture extension. In: Howard GC, Fast CR, editors. Drilling and production practices. Tulsa OK: American Petroleum Institute; 1957. p. 261–70.  
 [21] Bueckner HF. A novel principle for the computation of stress intensity factors. Z Angew Math Mech 1970;50(9):529–46.  
 [22] Rice JR. Some remarks on elastic crack-tip stress fields. Int J Solids Struct 1972;8(6):751–8.  
 [23] Kanninen MF, Popelar CH. Advanced fracture mechanics. The Oxford engineering science series, vol. 15. Oxford, UK: Oxford University Press; 1985.  
 [24] Rice JR. Mathematical analysis in the mechanics of fracture. In: Liebowitz H, editor. Fracture, an advanced treatise, vol. II. New York, NY: Academic Press; 1968. p. 191–311. [Chapter 3].  
 [25] Irwin GR. Analysis of stresses and strains near the end of a crack traversing a plate. ASME J Appl Mech 1957;29:361–4.  
 [26] Tada H, Paris PC, Irwin GR. The stress analysis of cracks, handbook, second edition, 2nd ed. Paris Productions Inc.; 1985.  
 [27] Simonson E, Abou-Sayed A, Clifton R. Containment of massive hydraulic fractures. Soc Pet Eng J 1978;18(1):27–32. [SPE 6089].  
 [28] Detournay E. Propagation regimes of fluid-driven fractures in impermeable rocks. Int J Geomech 2004;4(1):1–11.  
 [29] Nolte KG, Smith MB. Interpretation of fracturing pressures. J Pet Technol 1981;33(9):1767.  
 [30] Kovalyshen Y, Detournay E. A reexamination of the classical PKN model of hydraulic fracture. Trans Porous Media 2010;81(2):317–39.  
 [31] Peirce AP, Detournay E, Adachi JI. colP3D: a MATLAB code for simulating a pseudo-3d hydraulic fracture with equilibrium height growth across stress barriers <http://hdl.handle.net/2429/19969>; 2010.  
 [32] Barenblatt GI. Scaling, self-similarity, and intermediate asymptotics. Cambridge texts in applied mathematics, vol. 14. Cambridge, UK: Cambridge University Press; 1996.  
 [33] Kierzenka JA, Shampine LF. A BVP solver based on residual control and the MATLAB PSE. ACM Trans Math Software 2001;27(3):299–316.  
 [34] Kemp LF. Study of Nordgren's equation of hydraulic fracturing. SPE Production Engineering (SPE 19959), August 1990. p. 311–4.